Remote Sensing of Environment 231 (2019) 111255

Contents lists available at ScienceDirect

Remote Sensing of Environment

journal homepage: www.elsevier.com/locate/rse

Review

The legacy of the SIR-C/X-SAR radar system: 25 years on

Anthony Freeman[a,*], Manfred Zink[b], Ed Caro[a], Alberto Moreira[b], Louise Veilleux[a], Marian Werner[b]

[a] Jet Propulsion Laboratory, California Institute of Technology, Pasadena, CA 91109, USA
[b] DLR, German Aerospace Center, Microwaves and Radar Institute, 82234 Oberpfaffenhofen, Germany

ARTICLE INFO

Keywords:
SIR-C/X-SAR
Synthetic Aperture Radar
Polarimetry
Interferometry
Multi-frequency
Calibration
GPS Reflectometry

ABSTRACT

Twenty-five years ago, the two flights of the SIR-C/X-SAR Synthetic Aperture Radar (SAR) system on the Space Shuttle Endeavour blazed a trail towards the future with a series of radar system innovations — that nearly every spaceborne SAR flown since then has benefited from, and in some cases improved upon. Many of the SAR techniques adopted by SAR system designers worldwide as part of their toolkit, such as: ScanSAR, Spotlight mode, along-track interferometry, polarization diversity and polarimetry, polarimetric calibration, variable length and bandwidth pulses, and on-board processing, can trace their heritage back to this first-of-a-kind, civil-use SAR system. The electronic steering capability of SIR-C's phased array antenna, combined with the exquisite orbit track control provided by the Space Shuttle, paved the way for systematic mapping of the Earth's topography by the Shuttle Radar Topography Mission, and later by TanDEM-X. Some techniques, such as multi-frequency SAR, multi-frequency repeat-pass interferometry and onboard processing have yet to be fully exploited. The richness of the SIR-C/X-SAR data set has proved to be a treasure trove for opening up entirely new remote sensing techniques, such as Polarimetric SAR Interferometry (or PolInSAR), and GPS, now GNSS, reflections (also known as Signals of Opportunity), which were both demonstrated from archive data, years after the 1994 flights. The ground-breaking legacy of SIR-C/X-SAR lives on in the many SAR systems collecting data in Earth orbit today, and in those planned for the future.

1. Introduction

1.1. A brief history of the SIR-C/X-SAR system

The most advanced civil-use spaceborne SAR system of its time, the Spaceborne Imaging Radar-C/X-band Synthetic Aperture Radar (SIR-C/X-SAR) had its roots in a series of imaging radar missions that began with NASA's Seasat synthetic aperture radar in 1978 (Evans et al., 2005). Seasat was a single frequency (L-band with wavelength of 24 cm), single polarization, radar, with a fixed-look angle (23°). Next up in 1981 was the Shuttle Imaging Radar-A (SIR-A), which flew on the Space Shuttle Columbia, and was another L-band radar with a fixed look angle (Elachi et al., 1982). Mechanical steering for a multi-look angle capability was added and flown in 1984 as the SIR-B radar system (Cimino et al., 1986). In parallel, the German Aerospace Center (DLR, then called DARA) had also developed and flown an X-band (wavelength 3 cm) SAR known as the Microwave Remote Sensing Experiment (MRSE) on the Space Shuttle Columbia in 1983 (Dieterle and Schlude, 1982).

From these beginnings, SIR-C/X-SAR was conceived as a joint venture between NASA, the German Space Agency (DLR), and the Italian Space Agency (ASI) (Jordan et al., 1995). SIR-C/X-SAR provided increased capability over the prior Seasat, SIR-A, SIR-B and MRSE systems by acquiring images at three wavelengths: L-band, C-band (wavelength ~ 6 cm) and X-band. The L- and C-band radars could be tuned to select among several polarization options, and had the capability of full quad-polarized (or polarimetric) data acquisition. The X-band system, developed jointly by DLR and ASI, had VV polarization capability, transmitting and receiving vertically (V) polarized radar pulses. SIR-C/X-SAR also had a variable look angle, and could point towards look angles between 20 and 55° off nadir by electronic steering at L- and C-band, and mechanically at X-band. Experimental modes stretched to look angles as high as 65°. SIR-C/X-SAR flew on the Space Shuttle Endeavour in April and October of 1994, providing radar science data representative of two seasons.

* Corresponding author.
E-mail addresses: anthony.freeman@jpl.nasa.gov (A. Freeman), manfred.zink@dlr.de (M. Zink), Alberto.Moreira@dlr.de (A. Moreira).

https://doi.org/10.1016/j.rse.2019.111255
Received 28 March 2019; Received in revised form 31 May 2019; Accepted 7 June 2019

1.2. Science results

With over 5000 publications referencing the use of SIR-C/X-SAR data, the mission clearly has had a significant influence on active microwave remote sensing to understand and characterize the Earth system. Much has been written elsewhere about the science return from the SIR-C/X-SAR flights (Stofan et al., 1995; Öttl, 1997; Evans et al., 1997; Schmullius and Evans, 1997; Evans, 2006) but that is not the primary focus of this paper, which instead emphasizes the innovative, spaceborne SAR system techniques first demonstrated with SIR-C/X-SAR. Here we give a summary referencing the most frequently cited science results enabled by those techniques.

The science team was organized into sub-groups around several disciplines: Geology, Hydrology, Ecology, Oceanography, Electromagnetic Theory, Calibration and Rain/Interferometry. Data acquisitions and in situ calibration/validation efforts were focused at nineteen different 'supersites' geographically distributed across the globe. What the science team achieved across all of these disciplines, and at all these sites, was the validation of algorithms that generated geophysical data products from calibrated, multi-frequency, multi-polarization SAR backscatter data (Ranson et al., 1995; Dobson et al., 1995; Hess et al., 1995; Shi and Dozier, 1995; Dubois et al., 1995; Greeley and Blumberg, 1995; Mouginis-Mark, 1995; Beal and Monaldo, 1995; Moreira et al., 1995). An example of such a geophysical data product is the inundation map from part of the Manaus, Brazil supersite shown in Fig. 1. Other significant geophysical products include forest biomass estimates (Dobson et al., 1995), snow wetness (Shi and Dozier, 1995), soil moisture (Dubois et al., 1995) and surface wave fields in the Southern Ocean (Beal and Monaldo, 1995). The Calibration sub-group straddled the divide between science and engineering, producing fully calibrated data, along with calibration uncertainties (Klein, 1992; Zink and Bamler, 1995; Freeman et al., 1995; Sarabandi et al., 1995; Ponte and Vetrella, 1997; Fang and Moore, 1997; Fujita et al., 1998), for the other sub-groups to then confidently apply and validate their geophysical estimation algorithms.

Oceanographers found the data useful in studying surface features on the open ocean (Holt, 1998; Macklin and Stapleton, 1998; Monaldo and Beal, 1998; Melsheimer et al., 1998), including natural and man-made oil slicks (Masuko et al., 1995; Gade et al., 1998; Migliaccio et al., 2007). Snow hydrologists advanced their understanding of how microwaves can be used to probe the properties of snow packs (Shi and Dozier, 1997; Matzler et al., 1997; Shi and Dozier, 2000a; Shi and Dozier, 2000b). Scientists investigating microwave remote sensing of precipitation found quite a few examples in SIR-C/X-SAR data (Moore et al., 1997; Jameson et al., 1997). Land surface hydrologists mined rich veins of SIR-C/X-SAR data to investigate soil moisture variability (Wang et al., 1997; Macelloni et al., 1999; Narayanan and Hirsave, 2001) and wetlands (Pope et al., 1997; Pope et al., 2001; Alsdorf et al., 2001; Hess and Melack, 2003). Ecosystem scientists have applied SIR-C/X-SAR data to a diverse range of vegetation biomes (Kasischke et al., 1997). Researchers have reported estimates of biomass and carbon storage in Northern and temperate forests (Souyris et al., 1995; Ranson and Sun, 1997; Harrell et al., 1997; Bergen et al., 1998; Ranson et al., 2001); deforestation and secondary growth in tropical forests (Saatchi et al., 1997; Foody et al., 1997; Rignot et al., 1997; Yanasse et al., 1997); and land use classification and monitoring in agricultural regions (Pultz et al., 1997; Soares et al., 1997; Ferrazzoli et al., 1997; Pierce et al., 1994; Pierce et al., 1998; Zribi et al., 1997; Nagai et al., 1997; Paloscia, 2002). Volcanologists have found SIR-C/X-SAR data to be helpful in the study of both active and dormant volcanoes (Zebker et al., 1996; MacKay and Mouginis-Mark, 1997; Huadong et al., 1997; MacKay et al., 1998). Geologists found the data to be especially beneficial in revealing

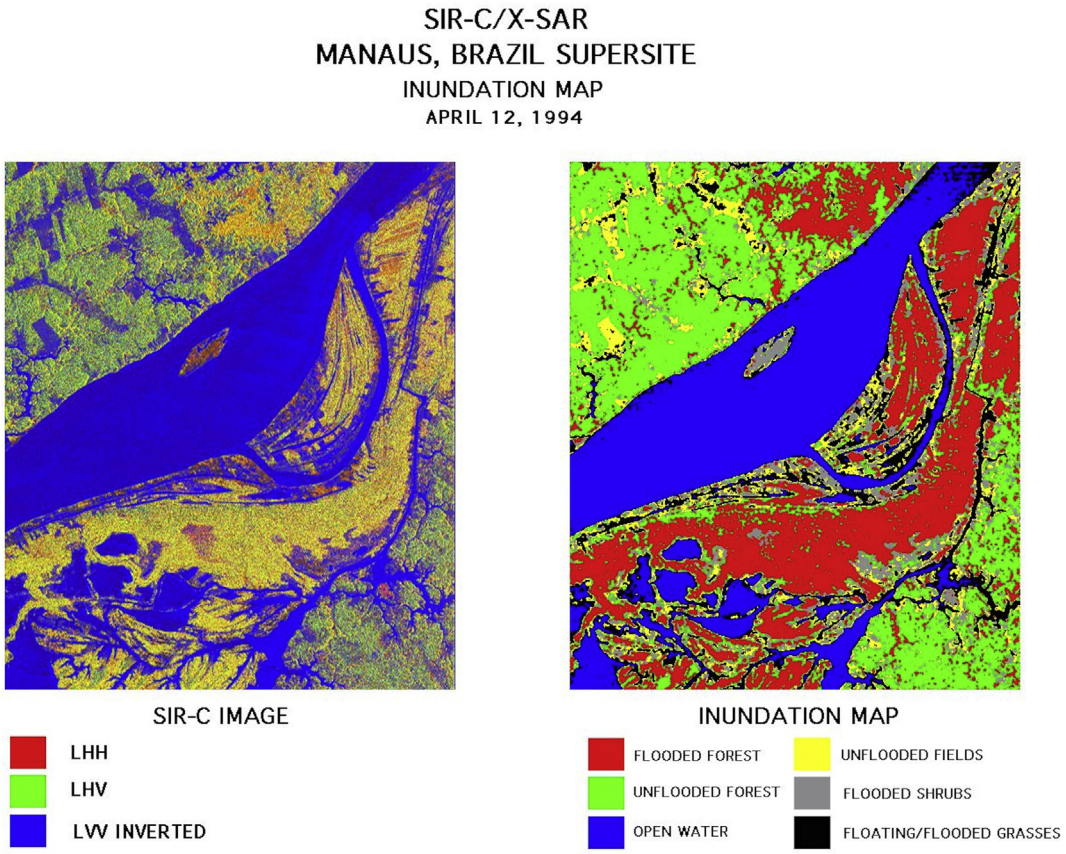

Fig. 1. Inundation map (right) of part of the Manaus, Brazil supersite in the Central Amazon, generated during the mission from multi-polarization L-band SIR-C data (left).

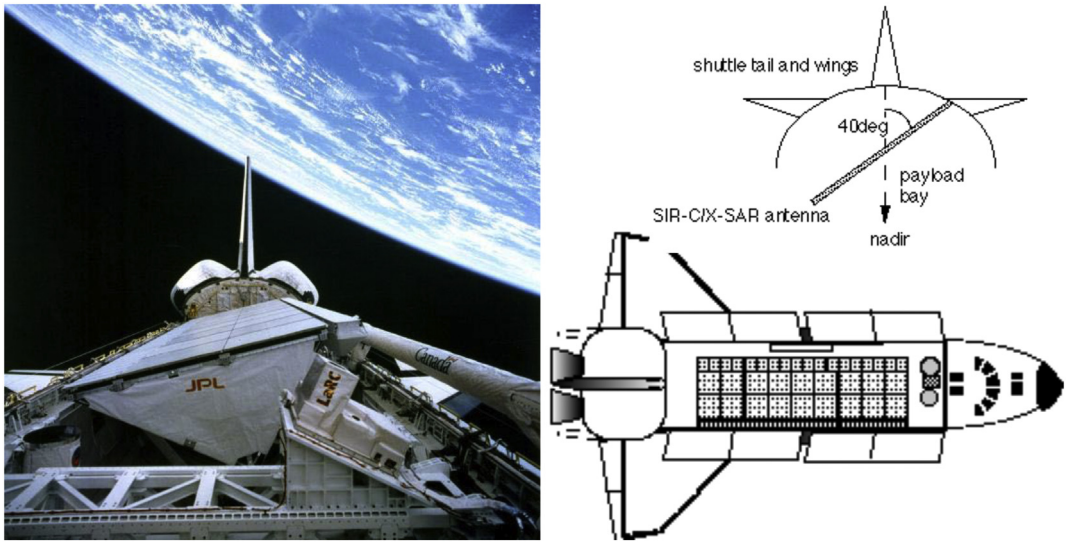

Fig. 2. The SIR-C/X-SAR system with its antennas pointed Earthwards in the cargo bay of the Space Shuttle Endeavour. On-orbit photo (left); cartoon sketches showing the configuration of the radar in the Shuttle cargo bay (right).

geologic features obscured by sand or vegetation cover (Kruse, 1996; Guo et al., 1996; Schaber et al., 1997; Weeks et al., 1997; Dabbagh et al., 1997; Stern and Abdelsalam, 1996; Abdelsalam and Stern, 1996; Kusky and Ramadan, 2002; Mchone et al., 2002). Cryosphere scientists have studied mid-latitude glaciers using SIR-C/X-SAR data (Forster et al., 1996; Albright et al., 1998; Floricioiu and Rott, 2001). New applications for the data, that emerged after the mission, include archaeology (Moore et al., 2006; Chen et al., 2015) and even prospecting for gold (Ramadan et al., 2001).

1.3. System description

SIR-C/X-SAR was the first multi-frequency, multi-polarization SAR system flown in space (Stuhr et al., 1995). Its 12 m by 4 m antenna and radar electronics modules were mounted on an aluminum support structure which nearly filled the Shuttle cargo bay (Fig. 2). The orbit altitude for both missions was roughly 225 km. On-orbit the Shuttle was oriented so that the mechanical boresight of the L- and C-band antennas was about 40° off nadir. Pointing over a wide range of look angles was achieved electronically via a phased array antenna at L- and C-band, and mechanically rotating the slotted waveguide antenna at X-band. All three wavelengths were pointed towards the same look angle for each data acquisition. Left- and right-looking imaging configurations were achieved by re-orienting the Space Shuttle at intervals throughout each mission.

As the Shuttle approached each supersite, the antenna was pointed so that the radar's footprint on the ground would cover it. The challenge then for the radar systems engineering team was to pre-determine the appropriate mode for the radar system, and set up the commands to execute it. Officially, the system had 23 modes to choose from (Stofan et al., 1995), but as can be seen from Table 1, there were in fact a very broad range of options available. Fortunately, some options were categorized as 'experimental' modes, and not routinely offered to the science team sub-groups. A limiting factor in SIR-C/X-SAR operations was the capacity of the onboard data recorders, which could accommodate 180 Mbps for the L- and C-band receivers, and 45 Mbps for the X-band. Taking this into account, the widest swath widths were obtained when operating with just one polarization at each wavelength; as additional polarizations were added swaths became narrower.

Data were acquired more or less continuously during each 10-day mission, with occasional breaks so the astronaut crew could reload the onboard tape recorders, where all of the data were stored for later processing on the ground. A limited amount of data was relayed to the ground in real-time through NASA's Tracking and Data Relay Satellite (TDRS), which allowed some very fast turnaround SAR data processing and calibration runs (Freeman et al., 1994), and for the science teams to test some of their algorithms during the mission.

Table 1
SIR-C/X-SAR radar system parameters, illustrating the wide variety of options available for any given data acquisition. Experimental modes are indicated by an asterisk.

Parameter	L-Band	C-Band	X-Band
Wavelength	0.235 m	0.058 m	0.031 m
Spatial resolution	15 and 30 m; 7.5 m*		
Swath width	15 to 90 km		15 to 60 km
Look angles	20 to 55 (65*)°		
Peak RF transmit power	4400 W	1200 W	1400 W
Transmit pulse length	33.8, 16.9, & 8.45 μs		40 μs
Bandwidth	10, 20 and 40* MHz		
Quantization	8 or 4 bits; (8, 4) BFPQ; offset video		4 or 6 bits; I and Q
Single-Pol modes	HH or VV		VV
Dual-Pol modes	(HH, HV), (VH, VV) and (HH, VV)		–
Quad-Pol modes (fully polarimetric)	HH, HV, VH and VV		–
StripMap mode	Yes		Yes
ScanSAR mode	Yes		–
Spotlight mode*	Yes		–
Along-track interferometry*	C-band V-pol only		–
Real-time on-board processing (OBP)*	C-band HH only		–

2. Radar system innovations

The 1994 SIR-C/X-SAR missions generated a series of firsts for a civil-use, spaceborne SAR system. What follows is a brief discussion of each of these innovations and their significance.

2.1. First electronically steerable, phased array SAR

Really two phased array systems (the L- and C-band antennas were independent of each other), the SIR-C antennas had a distributed feed network with Transmit/Receive (T/R) modules mounted on the backplane (Jordan et al., 1995). Separate feed networks and T/R modules

Table 2
Earth-orbiting, civil-use Microwave Remote Sensing systems flown since 1994 — arranged by launch year — that exploit techniques first demonstrated by SIR-C/X-SAR (Farr et al., 2007; Ahmed et al., 1993; Ruf et al., 2018; Desnos et al., 2000; Shimada, 2009, Fox et al., 2002; Di Lazzaro et al., 2008; Werninghaus et al., 2004; eoportal, 2019; Krieger et al., 2005; Misra et al., 2006; Lee, 2010; Snoeij et al., 2010; Spencer et al., 2009; Yokota et al., 2013; Cohen et al., 2017; eoportal, 2019a; Frulla et al., 2011; Iceye, 2019; Séguin, 2005). Note that although both SRTM and TanDEM-X benefited from the RPI for Topography demonstrated with SIR-C/X-SAR, the technique actually used on these missions is Single-Pass Interferometry (SPI).

Observing system	Launch date	Freq. band	Phased array	Multi-freq.	Multi-Pol	Full Pol	Scan-SAR	Spot-light	2-D OBP	ATI	Rapid Cal/ Val	RPI for Topo	Pol-InSAR	System perf.	GPS refl.
Radarsat-1	1995	C					•								
SRTM	2000	C, X	•	•	•							•			
Envisat ASAR	2002	C	•		•		•				•			•	
ALOS PalSAR	2006	L	•			•							•		
Radarsat-2	2007	C	•		•	•	•	•		•	•	•	•		
COSMO/ SkyMed	2007	X	•				•	•							
TerraSAR-X	2007	X	•		•		•	•			•		•		
RISAT-2	2009	X			•		•	•						•	
TanDEM-X	2010	X	•		•					•	•	•	•		
RISAT-1	2012	C	•		•										
KompSAT-5	2013	X	•		•		•	•						•	
ALOS PalSAR-2	2014	L	•		•	•	•	•					•	•	
Sentinel-1A/ B	2014/16	C	•		•						•				
SMAP	2015	L			•						•				•
CyGNSS	2016	L													•
ASNARO-2	2018	X			•		•	•						•	
NovaSAR-S	2018	S	•		•		•						•	•	
PAZ	2018	X	•		•		•	•			•		•		
SAOCOM-1	2018	L	•		•	•	•							•	
IceEye	2018	X												•	
Radarsat-RCM	2019	C	•		•	•	•	•			•		•	•	

fed the H and V channels which were connected to microstrip patch radiating elements on the front face of each antenna. This delivered the capability to transmit and receive both polarizations simultaneously. Phase shifters embedded in each T/R module could be programmed to electronically point the antenna pattern ± 23° in elevation, ± 2° in azimuth. Antenna feeds were divided into two branches (fore and aft) which were usually combined, but for C-band V-pol only could be fed separately into the receiver subsystems, enabling an experimental along-track interferometry (ATI) mode.

The innovation of using a SAR with a phased array enabled near-instantaneous antenna pointing changes, guaranteeing coverage of all the science supersites on nearly every overpass, and enabled new modes of operation, such as ScanSAR, Spotlight and ATI. An additional benefit of using distributed T/R modules, with low power amplifiers, instead of a single high-power amplifier (e.g. a Travelling Wave Tube Amplifier or TWTA), is that it reduces the losses in the feed network which would be considerable in the case of such a large antenna (Jordan et al., 1995). The flexibility and resilience that a phased array antenna affords have been incorporated into the design of many civil-use SAR systems that have flown since 1994 (Table 2).

2.2. First multi-frequency SAR

Combining all three wavelengths into one spaceborne SAR system had not been done before (or since). It allowed scientists to compare simultaneously acquired radar backscatter characteristics across frequencies using targets representative of the entire Earth, and select the appropriate frequency for a given set of science drivers for future missions, such as the Shuttle Radar Topography Mission (SRTM) (Werner, 2001; Farr et al., 2007) and TanDEM-X (Moreira et al., 2004; Krieger et al., 2007; Rizzoli et al., 2017). For example, if the goal is to study long-term surface deformation, L-band is preferred, since it leads to less decorrelation in vegetated areas (Rosen et al., 1996); whereas if the goal is to map surface topography, shorter wavelengths were seen to perform better (C- and X-band).

Fig. 3 illustrates how each of the three bands can provide different information about an area under investigation. The dark intrusion at the bottom of the X-band image at the lower left of Fig. 3 could easily be confused with low backscatter from flooding, since open water tends to produce similar results in SAR images, provided the water surface is smooth on the scale of the radar wavelength. But the L-band image at the lower right shows no corresponding area of lower backscatter, which means the observed dark area cannot be a surface feature, since anything that is smooth on the scale of the radar wavelength at X-band will also most certainly be smooth at L-band. This is exemplified by the dark, sinuous river feature that winds its way across both X-band and L-band images. Finally, the C-band image in the lower center frame of the figure provides the final clue, since the dark intrusion is reduced in area, and in degree of darkness. The observed image artifacts are caused by the presence of a tropical rain cell over this area of Western Brazil (called Rondonia), where such events are frequent (Danklmayer et al., 2009). The rain attenuates the X-band radar waves strongly, resulting in no visible return from the surface; less strongly at C-band; and has no visible effect on the L-band data. This is entirely consistent with what propagation theory predicts for the effect of rain cells on radar waves. With some additional knowledge added of the underlying surface backscatter, simultaneously acquired multi-frequency SAR data can be inverted to estimate precipitation rates, to detect hydrometeor phase, and to classify rain type (Jameson et al., 1997).

The sensitivity to vegetation biomass of each radar wavelength can also be seen in Fig. 3. Rectangular patches of undisturbed forest are bright in all three wavebands, and show up as salmon-colored in the

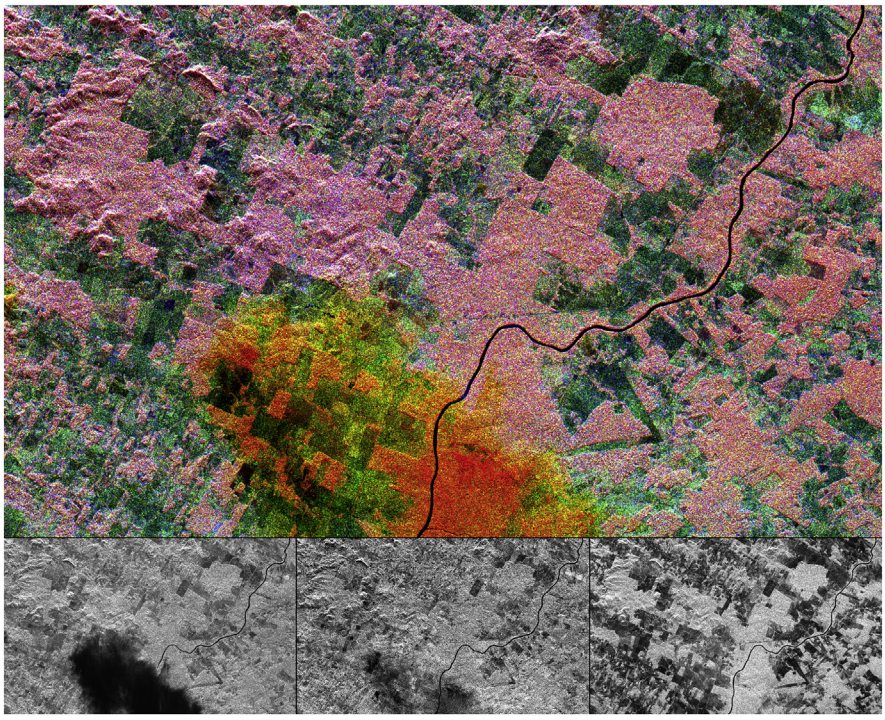

Fig. 3. Three-frequency SIR-C/X-SAR overlay of a rain event observed over an area of tropical rainforest in Rondonia, western Brazil. The image frames at the bottom are, from left to right, X-band VV-pol, C-band HV-pol, and L-band HV-pol. In the color composite image these same frames are color-coded blue, green and red. This example shows the increasing signal attenuation due to the rain with radar frequency in C-band and X-band, whereas the L-band is mostly unaffected. (For interpretation of the references to color in this figure legend, the reader is referred to the web version of this article.)

color composite image. All of the clear-cut areas tend to be dark in the L-band image; areas that are dark blue are dark in all three wavebands, indicating very low levels of vegetative cover, such as one would expect to see for grassland pastures. Areas that appear green in the color composite image have higher backscatter levels at C-band (but not at L-band), indicating intermediate levels of vegetation, e.g. scrubland where cleared forest is starting to grow back.

Researchers have had access to multi-frequency spaceborne SAR data since SIR-C/X-SAR, acquired over the same areas by, for example, ALOS PalSAR-2 (Shimada, 2009; Rosenqvist et al., 2014), Sentinel-1 (Snoeij et al., 2010; Potin et al., 2016) or Radarsat-2 (Fox et al., 2002; Séguin and Ahmed, 2009), and TerraSAR-X (Werninghaus et al., 2004; Werninghaus and Buckreuss, 2009). The difference is that these acquisitions are not contemporaneous, which introduces the extra dimension of temporal variability into the data. Precipitation (rain or snow) between acquisitions can change the radar backscatter; as can drought conditions, vegetation growth and senescence, land use changes, wind conditions (over water in particular), and atmospheric conditions. All of these confounding factors make interpretation of non-contemporaneous, multi-frequency SAR data much less straightforward than was the case for SIR-C/X-SAR.

2.3. First civil-use X-band SAR

MRSE was supposed to precede X-SAR as the first civil-use X-band SAR, but because of an on-orbit malfunction, that honor goes instead to X-SAR. The results from the 1994 missions showed that X-band SAR had value in mapping geophysical characteristics of the Earth's surface, beyond reconnaissance of targets of geopolitical interest (Gunter's Space Page, 1964). This realization led to a slew of X-band spaceborne SARs for civil-use, as can be seen in Tables 2 and 3.

2.4. First SAR with polarization diversity

The Seasat, SIR-A, SIR-B and MRSE SAR systems (Evans et al., 2005; Elachi et al., 1982; Cimino et al., 1986; Dieterle and Schlude, 1982) were all single-polarization systems, as were the European ERS-1 (Attema et al., 2000) and Japanese JERS-1 (Nomoko et al., 1991), already on orbit in 1994, and the Canadian Radarsat-1 which launched in 1995 (Ahmed et al., 1993). SIR-C could transmit horizontally polarized (H) or vertically polarized (V) radar pulses, and receive either H- or V-polarized echoes. The convention used is that HV means H-polarization transmit, V-polarization receive. SIR-C could therefore acquire multiple combinations of (HH, HV, VH and VV) polarizations at both L-band and C-band (Table 1). Results from the 1994 missions demonstrated the value of multi-polarization measurements in science investigations, and nearly every civil-use SAR launched since has incorporated this capability, either as dual- or quad-polarized imaging systems (Table 2).

2.5. First fully polarimetric SAR

The importance of measuring all four channels HH,HV,VH and VV coherently, i.e. with all polarimetric phases intact, was eloquently championed by the late Prof. Wolfgang Boerner (Boerner et al., 1988; Boerner et al., 1992; Boerner et al., 1998), and his work had a significant influence on the adoption of the fully polarimetric mode for SIR-C. In this mode, all four canonical elements of the Scattering Matrix (HH, HV, VH and VV radar echoes) were measured coherently and simultaneously, and it was possible to separate out the different physical scattering mechanisms contributing to the observed radar backscatter (van Zyl, 1989; Freeman and Durden, 1998). Mathematical decompositions of the scattering matrix into separate, often orthogonal components, provide a powerful tool for discriminating between and understanding the nature of surface features (Cloude and Pottier, 1996).

Fig. 4 is an example of how separation of scattering mechanisms in SAR polarimetry can help in interpreting SAR images. The L-Band image shown in the figure was acquired in April 1994 and is of a largely flat, agricultural polder in the Netherlands, just East of Amsterdam, which was a SIR-C supersite for Calibration and Ecology (land use) studies. Surface, double-bounce and volume scattering mechanisms estimated from the fully polarimetric SAR data are combined for each pixel, represented in color as blue, red and green, respectively. Dark blue pixels are areas where scattering from a smooth surface dominates, largely open water and a few of the fields in the center of the image which are probably bare soil. At the time of acquisition, most of the

Table 3
Microwave Remote Sensing systems in the planning or development stages (organized by nominal launch year) that make use of techniques first demonstrated by SIR-C/X-SAR.

Observing system	Nominal launch date	Freq. band	Phased array	Multi-freq.	Multi-Pol	Full Pol	Scan-SAR	Spot-light	2-D OBP	ATI	Rapid Cal/ Val	RPI for Topo	Pol-InSAR	System perf.	GPS refl.
Cosmo/ SkyMed G2	2019	X	•		•	•	•	•						•	
MicroXSAR	2020	X						•						•	
KompSAT-6	2020	X	•		•		•	•			•		•		
BIOMASS	2022	P				•					•		•	•	
NISAR	2022	S, L		•	•	•	•				•		•	•	
ALOS-4	2021	L	•		•	•	•	•					•	•	
Sentinel-1C/ D	2022/23	C	•		•						•			•	
Tandem-L	2025	L			•	•	•			•	•		•	•	
SNoOPI	2022	P													•
VERITAS	2025	X							•					•	
HRWS	2025	X	•		•	•	•	•		•	•			•	
Mars P-band SAR	2028	P			•	•								•	

Fig. 4. The Freeman-Durden decomposition applied to L-band SIR-C polarimetric SAR data over the Flevoland supersite, in the Netherlands. Blue = surface scattering; Red = double-bounce; and Green = Volume scattering. Areas in yellow have strong double-bounce scattering, mixed with volume scatter. (For interpretation of the references to color in this figure legend, the reader is referred to the web version of this article.)

agricultural fields were in fact bare soil, which show up as rectangles of lighter shades of varying degrees of blue, indicating different surface roughness patterns. Large areas of forest plantations appear green in the image (mostly due to volume scatter from the tree canopies). The suburban towns of Almere and Harderwijk appear mostly yellow in the image, indicating a mix of double-bounce and volume scatter. The double-bounce component is probably from right angles formed by streets and the sides of buildings. The volume scatter in this case could be from trees along leafy suburban avenues, or from scattering from buildings that are not aligned with the radar flight direction, and therefore exhibit non-reflection symmetry which generates significant HV-polarized returns (Yamaguchi et al., 2005; Ainsworth et al., 2008).

The field of Radar Polarimetry was given a significant boost by the SIR-C/X-SAR mission. For the first time, researchers had access to fully calibrated, polarimetric SAR data sets that covered large areas at similar look angles (Fig. 4). Previous airborne data had variable incidence angles across each image, which changes the scattering characteristics significantly (Freeman et al., 1992).

2.6. First ScanSAR

SAR designers had long sought ways to enhance the swath coverage obtained from a spaceborne SAR system so that larger areas could be accessed from orbit, and temporal revisit interval decreased. The impetus came mostly from the oceanographic scientists, who wanted more frequent, synoptic views of ocean features that cover larger scales than the typical 80–100 km swath images produced by Seasat, ERS-1/2, and JERS-1. Examples include the surface manifestation of major ocean currents such as the Gulf Stream, mesoscale eddies, surface wind patterns beneath typhoons and hurricanes, and sea ice extent. Using the electronic steering capability of SIR-C's phased array antennas to point the antenna footprint at multiple sub-swaths in elevation during a single pass over a target area, it was shown for the first time that this was indeed possible (Chang et al., 1995), using a technique known as ScanSAR (Tomiyasu, 1981; Moore et al., 1981), with the trade-off being reduced spatial resolution in the along-track or azimuth dimension.

The first ScanSAR image acquired by SIR-C/X-SAR is shown in Fig. 5. The image was acquired over the northernmost edge of the sea ice pack in the Weddell Sea, off Antarctica. The transition from open ocean (blue) at the top of the image to sea ice (green) at the bottom is clearly visible. Also seen are two large ocean circulation features, which are eddies. Oceanographers study eddy processes in this region because they play an important role in the circulation of the global ocean and the transportation of heat towards the pole.

This demonstration of obtaining wide swath coverage by rapidly

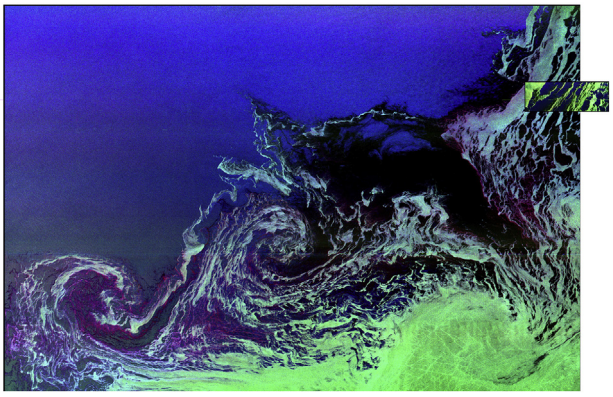

Fig. 5. First SIR-C/X-SAR ScanSAR image of ocean and sea ice features in the Weddell Sea near Antarctica. This image was acquired in October of 1994. The image is multi-frequency (C– and L-band) and multi-polarization (VH and VV), with dimensions 240 km × 350 km. The small inset image at top right is a narrower-swath SIR-C/X-SAR image acquired the following day, illustrating the huge difference in swath coverage between the ScanSAR mode and a more typical multi-channel SIR-C/X-SAR acquisition.

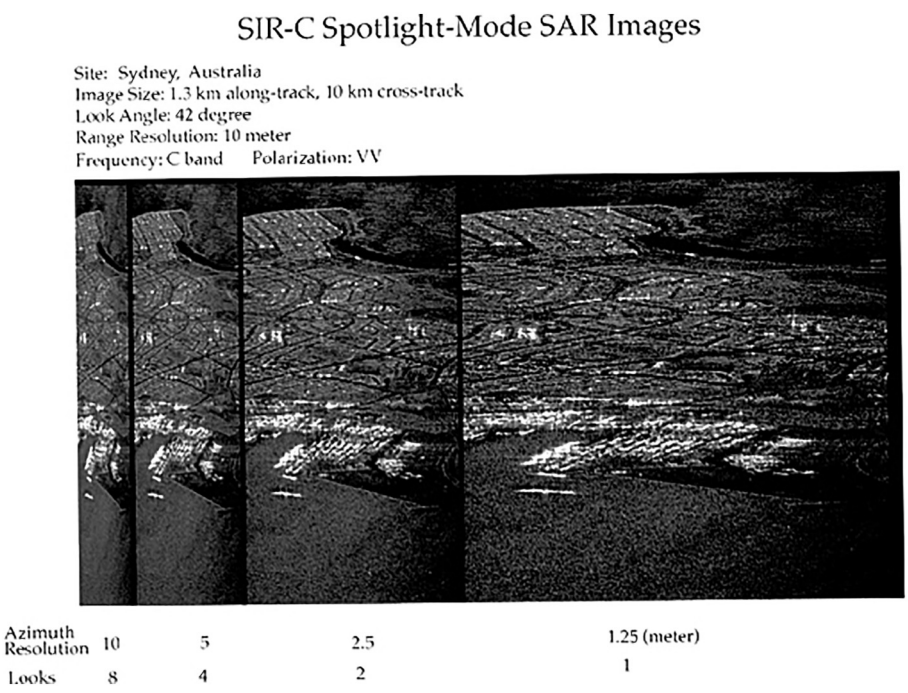

Fig. 6. First C-Band VV polarization Spotlight SAR image from SIR-C/X-SAR data acquired over Sydney, Australia). Image dimensions are 1.3 km × 10 km. Spatial resolution is ~1.25 m in azimuth, ~10 m in range in the frame to the far right. Pixels have been multi-looked or spatially averaged in azimuth by factors of 2, 4 and 8 in the frames to the left.

switching between sub-swaths in elevation was an enabling capability for the SRTM mission (Farr et al., 2007), and has been adopted in many subsequent spaceborne SAR systems (Table 2). Since SIR-C/X-SAR, SAR designers have found ways to improve on the ScanSAR technique. Due to the so-called scalloping effect (Bamler, 1995) ScanSAR images are impacted by systematic SNR variations in the azimuth direction. To overcome this problem the Terrain Observation by Progressive Scans (TOPS) mode combines scanning in elevation with backward to forward steering (opposite to spotlight mode) of the beam in the flight direction (de Zan and Monti Guarnieri, 2006).

2.7. First spotlight SAR

By electronically steering the phased array antenna in azimuth, so the footprint remains pointed towards a particular target area, the resulting data can be processed to obtain higher azimuth resolution than the classical half the antenna length (L/2) limit. This was demonstrated via a Spotlight mode SIR-C data acquisition over Sydney, Australia during the second mission (Fig. 6).

Processing of SIR-C Spotlight mode data is described in (Lanari et al, 2001). This experimental mode for the SIR-C/X-SAR mission has since been incorporated into the design of several SAR systems, for use when high spatial resolution is really needed. For example, the staring spotlight mode on TerraSAR-X fully exploits the steering capabilities and can provide azimuth resolutions down to 20 cm (Mittermayer et al., 2014).

2.8. First onboard 2-D SAR and real-time processing

The Johns Hopkins University Applied Physics Laboratory (JHU/APL) added an electronics box to the SIR-C radar electronics that tapped off the C-band HH receive chain and processed the data acquired in real-time, turning the resulting focused SAR images into wave spectra for downlink through NASA's Tracking and Data Relay Satellite (TDRS) (Beal and Monaldo, 1995; Beal et al., 1991). This introduction of Onboard processing (OBP) was well ahead of its time, and to our knowledge this innovation has been adopted by no civil-use SAR system designed and built since (Table 2).

A ground-based real-time processor was developed for the X-SAR system, which was integrated in the mission control facilities in the Space Center Houston. Depending on the availability of TDRS relay, the X-SAR raw data were downlinked and processed with an azimuth resolution of 16 m to 60 m using a simplified SPECAN (Spectral Analysis) algorithm. The real-time processing allowed a quick cross-check of the data quality, optimization of the radar instrument parameters and provided fast access to the data by the mission scientists. The images were also displayed on NASA television in real-time during the mission.

2.9. First along-track interferometer

On both flights of SIR-C/X-SAR, the ATI mode was exercised over the Gulf Stream supersite (Mango et al., 1995), with a phase center offset of half the physical antenna length – 6 m. In situ surface current measurements were collected to compare with ocean surface motion estimates from the ATI data. Because of the short baseline between the phase centers, the sensitivity of these ATI measurements of opportunity was somewhat limited, but the general feasibility of current measurements from satellites using SAR interferometry was demonstrated (Romeiser et al., 2002). The split antenna concept has been adopted on TerraSAR-X and TanDEM-X to provide ATI measurements and an experimental fully polarimetric mode (Werninghaus and Buckreuss, 2009; Gabele et al., 2009; Bueso-Bello et al., 2017).

2.10. First rapid-turn-around Cal/Val

Data from the Seasat, SIR-A, and SIR-B missions were not routinely calibrated. Quick-look images were available for ERS-1 and JERS-1, but users often had to wait many months to get their hands on fully calibrated data products. During both SIR-C/X-SAR missions, rapid response teams were engaged in processing and turning out the first calibrated data products within hours of their acquisition (Zink and Bamler, 1995; Freeman et al., 1995). A multitude of calibration devices including corner reflectors, transponders, tone generators and signal receivers were deployed at several of the supersites distributed around the world (see example in Fig. 7). The objective was to get calibrated data acquired over the supersites into the hands of science investigators as quickly as possible, so they could validate their algorithms and generate geophysical parameters (Stofan et al., 1995). This practice became more common following SIR-C/X-SAR (Table 2).

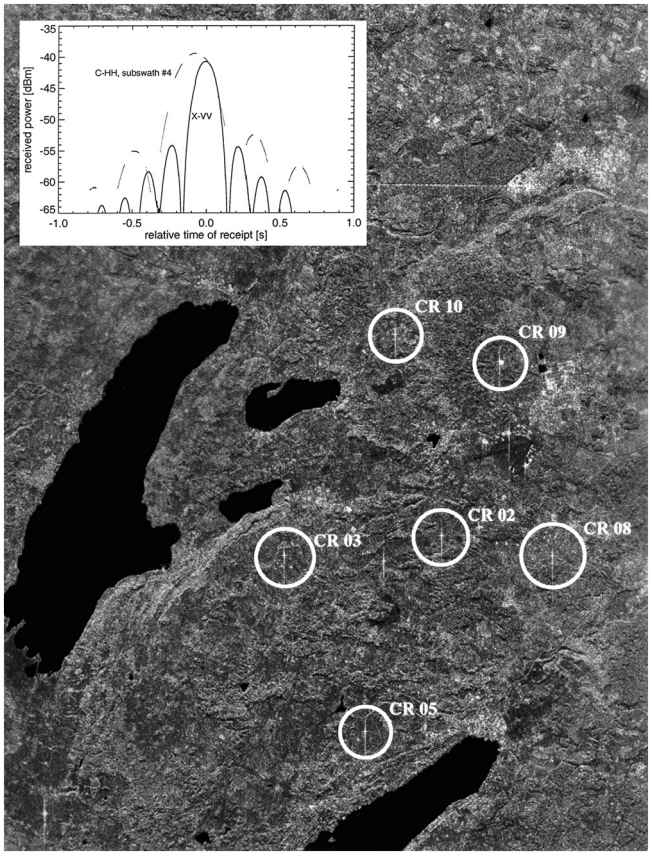

Fig. 7. X-SAR image acquired over the calibration supersite around DLR Oberpfaffenhofen, Germany showing the point target response of six 3-m trihedral corner reflectors. The insert shows azimuth cuts through the C-band and X-band antenna patterns measured by ground receivers (gaps in the C-band data are due to the ScanSAR operation). The observed slight time offset between the peaks, corresponding to a squint of about 0.1°, was not a problem during the SIR-C/X-SAR mission, but later became an issue for SRTM that was addressed by electronic steering of the second antenna mounted on the tip of the boom (Geudtner et al., 2002).

2.11. First topographic mapping using Repeat-Pass Interferometry (RPI) at optimum angles

Repeat-Pass Interferometry was demonstrated using Seasat, ERS-1 and JERS-1 data prior to SIR-C/X-SAR, but none of these systems were set up for optimum topographic mapping. In the case of Seasat and ERS-1, with a fixed look angle of 23° from nadir, the resulting images in areas of significant topographic relief had too much layover and shadow. JERS-1 had a more favorable look angle of 35°, but the system signal-to-noise ratio and orbit track repeatability and knowledge were unsuitable. On the last three days of the second SIR-C/X-SAR flight, the Shuttle crew were able to adjust and lock down their orbit to repeat ground tracks to within about 50 m. This enabled long swaths of RPI data (Fig. 8) at all three wavelengths, with a baseline separation optimized for topographic mapping to be acquired and processed (Lanari et al., 1996; Rosen et al., 2000).

This paved the way for SRTM single-pass interferometry (SPI) data processing in 2000, to produce a near-global Digital Elevation Model (DEM) with 30 m postings, and 10 m height accuracy (Farr and Kobrick, 2000; Werner, 2001; Farr et al., 2007). X-SAR RPI and the experience DLR gained with X-band topographic mapping on SRTM led to an even better global DEM (12 m postings, 2 m height accuracy) produced by the TanDEM-X mission starting in 2010 (Moreira et al., 2004; Krieger et al., 2007; Zink et al., 2014). TanDEM-X again used the SPI approach, but from two separate platforms in bistatic radar operation, flying in formation with adjustable baseline geometry.

2.12. First multi-frequency RPI for surface deformation

The SIR-C/X-SAR missions enabled RPI studies of surface deformation over two timescales: the six months between the two Shuttle flights, and the day-to-day revisit during the orbit track lock-down period at the end of the second mission. Comparing across frequencies, the results indicated that longer wavelengths suffered less from decorrelation between observations in vegetated areas (Rosen et al., 1996; Lee et al., 2000). Multi-frequency, multi-pass coherence maps in non-vegetated areas, for example Fig. 9, were seen to provide better maps for geologic interpretation than SAR images alone (Coltelli et al., 1996).

2.13. First demonstration of several system performance enhancements

The first generation of spaceborne SARs suffered from severe dynamic range problems. JERS-1 for example had 3-bit Analog-to-Digital convertors (ADCs) with a variable gain amplifier in front, to try to maintain the power level of the received echoes in the 'sweet spot' for the ADCs. Radarsat-1 had 4-bit ADCs, and ERS-1 had 5-bit ADCs. The dynamic range of a perfectly engineered ADC is roughly the number of bits multiplied by 6 in dB. This can be lower than the dynamic range of the observed backscatter within the received radar echoes, so ERS-1, JERS-1 and Radarsat-1 all suffered to a degree from ADC saturation effects which led to distortion in the radar measurements (Meadows, 1994). In addition, all three generated In-Phase and Quadrature (I/Q) channels which were digitized separately. Since the I and Q channels were never truly orthogonal, this introduced an extra complication into the calibration of SAR data from these systems.

The SIR-C receiver system design incorporated 8-bit ADCs, with ~48 dB dynamic range, and the transmitter had a variable pulse width to adjust the expected SNR for observations over different terrain types (e.g. open ocean, forested areas, grassland and farmland, desert, etc.). The radar also had variable bandwidth settings (Table 1) and used an offset video receiver (one channel instead of the two needed for I/Q).

Due to the low orbital altitude (~225 km) of the Space Shuttle and the high peak power available, the thermal noise-equivalent sigma-zero was expected to be very low for all three radars (−40 dB at L-band; −35 dB at C-band; and − 22 dB at X-band according to Jordan et al., 1995). Most SIR-C data-takes used the (8, 4) Block Floating Point Quantization (BFPQ) scheme, and the round-off error introduced by the BFPQ step tended to define the image noise floor at about 18 dB below the average backscatter level in the scene. In at least one case, a very low backscatter scene was imaged using 8-bit quantization and the noise floor was estimated at −50 dB for L-band and − 35 dB for C-band (Freeman et al., 1995). X-SAR data too had much lower noise floors than advertised, ranging from −27 to −44 dB as seen on-orbit (Zink et al., 1995).

Because of all these enhancements, the radiometric quality of SIR-C/X-SAR data were very high — and as faster 8-bit ADCs, BFPQs, digital pulse generators, and offset video receiver designs have become more prevalent, later generation SAR systems have risen to similar standards of quality (Table 2).

2.14. First acquisition of PolInSAR data

Very few data sets were acquired in full polarimetric mode during the 3-day orbit lockdown on the second SIR-C/X-SAR mission, but serendipitously it turned out that would be enough to demonstrate the validity of an entirely new technique in radar remote sensing: Polarimetric SAR Interferometry, or PolinSAR (Cloude and Papathanassiou, 1998). PolInSAR is a very powerful tool for estimating forest height, and to first order, the structure of vegetation canopies (Cloude et al., 2003; Li et al., 2003), as seen in Fig. 10. It is a foundational technique for the European Space Agency (ESA)'s future

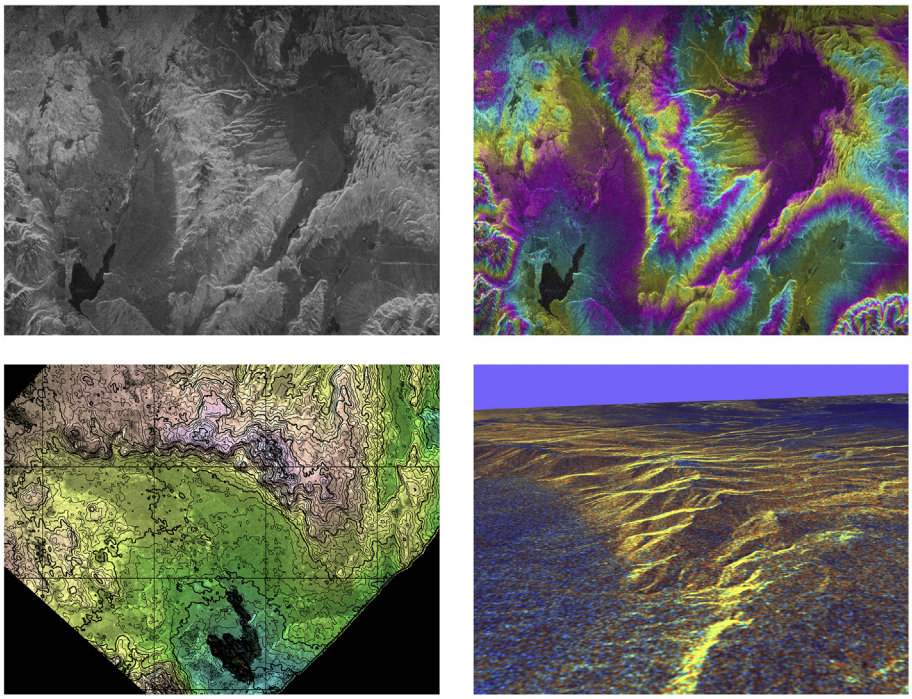

Fig. 8. RPI for topographic mapping example from the second mission, acquired over Long Valley, CA. Radar backscatter image (top left): radar interferogram (top right); DEM derived from the interferogram (bottom left); and perspective view of the DEM (bottom right).

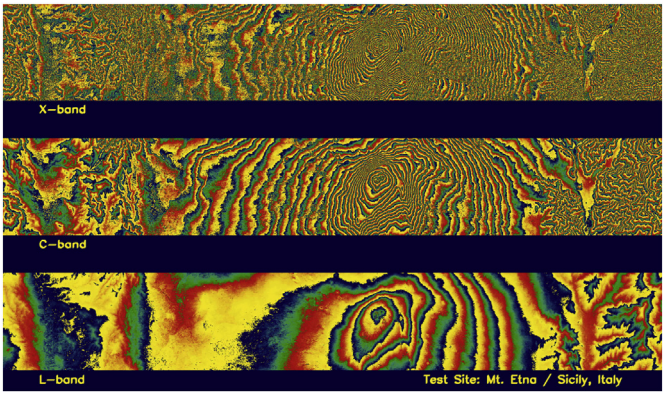

Fig. 9. Multi-frequency interferograms from SIR-C/X-SAR acquired over Mt. Etna, Italy, showing the differences in coherence between X-band (top), C-band (middle), and L-band (bottom) (Moreira et al., 1995).

BIOMASS mission (Le Toan et al., 2011; Quegan et al., 2019), NASA and ISRO's future NISAR mission (JPL, 2019), and for DLR's planned Tandem-L mission (Krieger et al., 2010; Moreira et al., 2015).

2.15. First GPS reflection measurement from space

Another, somewhat unexpected, result from SIR-C/X-SAR was the first measurement of L-band Global Positioning System (GPS) signals reflected from the ocean surface (Lowe et al., 2002). A re-analysis of archived SIR-C L-band data discovered data-takes that contained a strong, bistatic specular GPS reflection from a relatively smooth ocean. This paved the way for NASA's Cyclone Global Navigation System Satellites (CyGNSS) mission, which routinely uses this technique to estimate the strength of ocean surface winds and other surface phenomena from GPS reflections (Ruf et al., 2018). The technique is now widely known as GPS Reflectometry or GNSS Reflectometry.

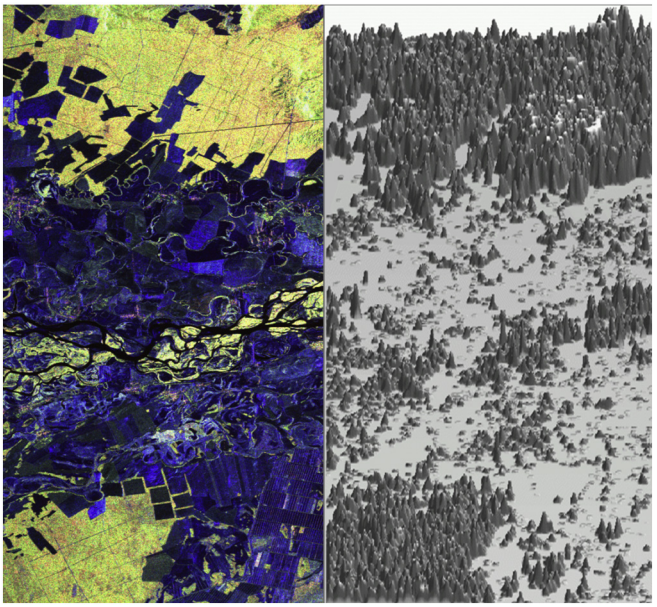

Fig. 10. Perspective view (right) of a boreal forest in Siberia generated from PolInSAR data, and corresponding multi-polarization L-band SAR image (left) from SIR-C/X-SAR, showing the potential of this new technique for estimating the forest height.
Image courtesy Shane Cloude/Kostas Papathanassiou (Cloude and Papathanassiou, 1998).

3. SAR systems after SIR-C/X-SAR

In addition to the innovations discussed above, a lot of lessons were learned during the SIR-C/X-SAR missions, which were freely and openly shared with the SAR community, e.g. (Freeman et al., 1996). The following addresses some of those lessons, and discusses their influence on the design of SAR missions that have flown after SIR-C/X-SAR, and others that are in the pipeline for the future (Table 3).

3.1. Concept of operations

The concept of operations (ConOps) built around targeting super-sites on each and every pass was extremely valuable for Cal/Val of the data and for testing algorithms used to generate geophysical products. In some cases, however, a higher science return may have been possible by using instead a "mow-the-lawn" ConOps, a scenario in which area coverage is systematically built up by mosaicking together data strips acquired on successive orbit passes. This lesson was incorporated into the design of the JERS-1 Multi-Season Amazon Mapping Study (JAMMS) in 1995/6 (Siqueira et al., 2000; Rosenqvist et al., 2000), and the JPL mission design for the RADARSAT Antarctic Mapping Project in 1997 (Jezek et al., 1996; Jezek, 2008). And, of course, SRTM (Farr et al., 2007) and TanDEM-X (Krieger et al., 2007) and other systematic global mapping SAR missions have very successfully adopted this same mow-the-lawn approach (e.g., ALOS-2 and Sentinel-1A/B).

3.2. Platform pointing

The Space Shuttle Endeavour was in many respects an ideal platform for the SIR-C/X-SAR missions: power for payload operations was plentiful, the payload mass and volume allocations were huge, and the skill of the astronaut crew in flying "locked-down" orbit tracks between missions has already been noted. There was just one area where the platform's performance was less than optimal: pointing. The onboard Digital Autopilot was capable of controlling Space Shuttle pointing by the selection of different attitude and attitude rate deadbands (Galvez et al., 2019), and for SIR-C/X-SAR the preferred values were at the lower end: ± 1.0° for attitude and ± 0.02° for attitude rate. Typical pointing knowledge requirements for today's SAR systems are one-tenth of the antenna beamwidth, which for SIR-C/X-SAR at C-band and X-band in the along-track (azimuth) dimension would have been 0.3 and 0.14°, respectively. This discrepancy between desired and actual performance meant that SAR system engineers had to derive some very clever approaches using Doppler tracking — based on the SAR data itself — to determine, post-acquisition, where the SIR-C/X-SAR antennas were actually pointing (e.g. Li et al., 1985; Madsen, 1989; Chang and Curlander, 1992; Moreira, 1992), which would allow the data to be properly processed. Today's free-flying spacecraft platforms have much better pointing knowledge and control, down to the milli-arcsecond level if necessary (Blackmore et al., 2011), obviating the need for most of the SAR data-based methods.

3.3. Design of Polarimetric SAR systems

Spaceborne polarimetric SARs flown to date have predominantly been implemented as experimental add-on modes to existing designs for single-polarized or dual-polarized systems. Lessons learned on the design and calibration of SAR systems specifically for fully polarimetric modes were captured in (Freeman, 2009), and are summarized here:

1) The effective Pulse Repetition Frequency has to be increased by a factor of 2 over conventional single- or dual-polarized SAR systems;
2) The length of the SAR antenna should be increased, if possible, to compensate for the reduced ambiguity-free swath due to 1);
3) Changing to a circular transmit, linear receive polarization basis may result in more balanced range ambiguities, so after polarization synthesis to retrieve the more commonly used HH, HV, VH and VV backscatter signatures the cross-pol HV and VH terms are not dominated by ambiguous like-pol returns. Recent studies show, however, that the ambiguity suppression should be investigated for each system design and imaging geometry when estimating the total ambiguity levels in range and azimuth (Villano et al, 2017);
4) System reciprocity (transmit behavior similar to receive) cannot be assumed; it must be demonstrated. If the system is not reciprocal, corrections should be applied to the data;
5) Minimizing antenna cross-talk in the along-track direction results in the best cross-talk performance at the system level;
6) Polarimetric calibration can be greatly simplified if system cross-talk can be reduced to negligible levels.

These lessons have been applied to the design of a P-band (68 cm wavelength) SAR designed to operate in orbit at Mars (Campbell et al., 2004; Campbell et al., 2004a), and also informed that of ESA's BIOMASS SAR system (Le Toan et al., 2011; Quegan et al., 2019).

Some SAR designers have begun to adopt compact or hybrid polarization architectures which have only two measurement channels (Souyris et al., 2005; Raney and Freeman, 2009), but are almost as rich in information as full polarimetry (e.g. Truong-Loi et al., 2009), and allow less constrained swath coverage than was the case for SIR-C/X-SAR. SIR-C/X-SAR data provided fully polarimetric reference data sets against which to test such approaches. NISAR, RISAT-1 and the Radarsat Constellation Mission, for example, have all incorporated Compact-Pol modes (eoportal, 2019b; Rao et al., 2016; Charbonneau et al., 2010).

3.4. Ionospheric propagation

Because of the low altitude of the Shuttle platform, ionospheric propagation had no expected or noticeable effect on SIR-C/X-SAR measurements and on polarimetric SAR calibration in particular. However, as early as 1994, there was interest in a free-flying version of SIR-C, which would have to be placed in a higher orbit, above most of the ionosphere. Research was initiated to examine the expected effects of ionospheric propagation, especially at the longer L-band wavelength, and at even lower frequencies such as P-band. The initial focus was on degradation in image quality due to group delay and pulse broadening effects in the highly dispersive ionosphere in the range direction; and lack of coherence to form a synthetic aperture due to ionospheric turbulence in the along-track direction (Ishimaru et al., 1999). This work was extended to include the effects of both horizontal and vertical ionospheric inhomogeneities in (Liu et al., 2003), and later to address propagation effects at VHF wavelengths (Freeman et al., 2017). It was also realized early on that Faraday rotation could significantly distort polarimetric SAR measurements at the longer wavelengths (Ishimaru et al., 1999; Wright et al., 2003; Freeman and Saatchi, 2004).

Subsequent longer-wavelength SARs flying in higher orbits would have to adapt the algorithms used for SIR-C polarimetric calibration to deal with ionospheric effects, particularly Faraday rotation, as discussed in (Freeman, 2004). SIR-C polarimetric data was used to simulate the effects of Faraday rotation and then the performance of algorithms to correct for them. Thanks to the openness of the Japanese ALOS PalSAR (and later ALOS PalSAR-2) team in sharing data and information about their system, viable approaches for polarimetric calibration that account for Faraday rotation were quickly identified and verified (Meyer and Nicoll, 2008; Shimada et al., 2009; Freeman et al., 2009). Such techniques will prove invaluable again when the P-band (68 cm wavelength) BIOMASS polarimetric SAR system is launched in ~2022 (Le Toan et al., 2011; Rogers and Quegan, 2014; Quegan et al., 2019), which is expected to experience severe (many 10's of degrees) Faraday rotation, as well as other ionospheric distortion effects (Kim et al., 2017). These techniques will also help ensure rapid turnaround in calibrating polarimetric SAR measurements from the planned NISAR (JPL, 2019) and Tandem-L missions (Krieger et al., 2010; Moreira et al., 2015).

3.5. Wide-swath, high-resolution systems

The successful acquisition of ScanSAR data led to a breakthrough in providing wide-swath, and therefore more frequent, coverage of large regions of the Earth (Desnos et al., 2000; Fox et al., 2002). The key trade-off, known even before SIR-C/X-SAR, has always been that

ScanSAR data yields only modest (typically 100 m or greater) spatial resolution. This will be remedied by future missions such as NISAR and Tandem-L, which have adopted a new technique developed by JPL and DLR, known as SweepSAR: a Scan-on-Receive architecture with a one-dimensional, phased array feed combined with a large (and light-weight) reflector antenna. SweepSAR permits wide-swath data collection, while at the same time providing full polarimetry and fine spatial resolution of order 10 m (Freeman et al., 2009a). Another technique, called Multiple Azimuth Phase Centers (MAPS), splits the antenna in the flight direction, so that each phase center is sampled by separate receivers. The additional samples allow reconstruction of the azimuth spectrum and control of ambiguities even at a lower Pulse Repetition Frequency (PRF), resulting in a wider echo window and swath width (Gebert et al., 2009).

3.6. Smaller, lighter antennas

With its huge dimensions of 12 m × 4 m, the SIR-C/X-SAR antenna is by far the largest civil-use SAR antenna flown to date, and the fact that it was a phased array at L- and C-band made it very heavy (3350 kg according to Jordan et al., 1995). A couple of questions the SAR designer often has to answer are: can you make the antenna smaller, and lighter? SIR-C data collected in experimental modes at very high look angles (e.g. 63°) helped answer the first question with a qualified yes (Freeman et al., 2000). The answer to the second question is also yes, but one has to give up some performance in either spatial resolution or ground swath (or both). With that proviso, it is certainly possible to design a SAR system that fits within a Smallsat form factor (< 300 kg total mass), and take advantage of the ongoing revolution in miniaturizing spacecraft (Freeman, 2018). Commercial operators like Finland's IceEye and Japan's NEC Corporation have already demonstrated and put this into practice with Smallsat SARs on orbit that are returning quality SAR images (Bird et al., 2013; Yokota et al., 2013; Iceye, 2019), and more are on the way (Filippazzo and Dinand, 2017; Saito et al., 2018; Capella Space, 2019). The trend towards SmallSat solutions thus far has resulted in X-band SAR systems that provide high resolution (a few meters), single-polarization imagery in all weathers, but longer wavelength systems are under consideration (Freeman and Chahat, 2017).

3.7. On-board processing (OBP)

One of the innovations demonstrated during SIR-C/X-SAR that remains under-exploited is onboard SAR processing (Tables 2 and 3). There are several explanations that can account for this. The first is that to preserve the full phase coherence in the data (for use in RPI for example), there is often not much (if any) data reduction from the 'raw' (as acquired) data format to the fully processed (complex) SAR image. Secondly, science users of SAR data often insist on each and every bit of the data collected being returned, so they can squeeze every last drop of science value from it. Thirdly, having access to the raw data does give flexibility in the format and quality of the final image product, in terms of number of looks, spatial resolution, geometric projection, calibration, etc. Finally, onboard processors with the appropriate throughput capacity have, until recently, been relatively expensive, massive and power-hungry.

The tide may yet turn for OBP on Earth-orbiting SARs as smaller, lightweight processors become available, and Smallsat SAR operators focus their attention on more application-oriented users, who have more interest in the information SAR systems can provide than in the underlying data. JPL (in collaboration with DLR and ASI) have recently proposed the VERITAS Venus-orbiting science mission, which would carry an InSAR payload known as VISAR (Hensley et al., 2015). With a fixed baseline similar to SRTM (but much shorter), VISAR's two SAR antennas would collect Single-Pass Interferometric SAR data, and use OBP to reduce it to the level of an interferogram (Figs. 8 and 9), which can be spatially averaged (multi-looked) to reduce the data volume dramatically (by a factor of up to a 1000). For planetary scientists this modification of the raw SAR data is seen as not just acceptable, but highly desirable, since it would result in the return of the highest-value data set – global surface topography at similar spatial scales to SRTM - to help them fill in the missing pieces in the evolution of Venus' surface (Freeman and Smrekar, 2015).

3.8. Tomography

The demonstration of PolInSAR using SIR-C/X-SAR data was so successful, it inspired researchers at DLR to introduce an entirely new technique called SAR Tomography, which can be thought of as PolInSAR with a new degree of freedom; multiple baseline separations. The concept of SAR tomography evolved in the late 90s after DLR had already gained experience with PolInSAR data acquisition and information retrieval by means of several flight campaigns using its airborne multi-frequency, multi-polarimetric SAR system. The airborne demonstrations were based on multiple repeat-pass tracks separated by a few tens of meters. SAR Tomography is an improvement over the single-baseline PolInSAR technique demonstrated with SIR-C/X-SAR because it can provide much better insights into the 3-D structure of vegetation canopies, resolving several different scattering layers at multiple heights (Reigber and Moreira, 2000; Tebaldini, 2010). With enough spatial resolution, SAR Tomography can also be used to reveal the complex 3-D structure of urban and forested terrain, as demonstrated using TanDEM-X data (Zhu and Bamler, 2010; Fornaro et al., 2012; Nannini et al., 2019). SAR Tomography is a core element of ESA's upcoming BIOMASS mission (Quegan et al., 2019), which when it launches in 2022 will be the first systematic use of this technique in space. Tandem-L will also feature tomography as an operational technique that will be used to derive 3-D structure information in forests and ice (Moreira et al., 2015).

3.9. Signals-of-Opportunity

Another under-exploited innovation resulting from SIR-C/X-SAR (Table 3) is the use of reflected Signals-of-Opportunity such as GPS to measure variations in geophysical properties of the Earth's surface (Lowe et al., 2002). NASA's CyGNSS mission (Ruf et al., 2018), which consists of 8 Smallsats flying in a 'string-of-pearls' formation, each mounted with GPS receivers on the top and bottom (nadir) decks of the spacecraft, has demonstrated the promise of this new remote sensing technique. Signals-of-Opportunity from existing microwave satellite transmissions cover all parts of the Radio Frequency spectrum, and open up the possibility of high temporal frequency measurements of geophysical parameters such as soil moisture; sea surface height; ocean vector winds; snow water equivalent; root zone soil moisture; and vegetation water content (Shah et al., 2018). NASA recently selected the SigNals-Of-Opportunity P-band Investigation (SNoOPI) — a CubeSat project pathfinder for measuring two of these environmental variables using reflected P-band Signals-of-Opportunity (Purdue, 2019).

4. Summary and discussion

Following its two ground-breaking flights in 1994, SIR-C/X-SAR has had a profound impact on today's active microwave remote sensing systems, SARs in particular, which is expected to continue into the future. SIR-C/X-SAR's science results laid down the fundamentals for characterizing the surface of the Earth using radar backscatter images collected from orbit, serving as a foundation for analysis of data produced by the many satellites now in operation (Table 2). The science was enabled by the introduction of a series of innovative radar techniques that have been incorporated into the design of today's SAR systems, and in some cases improved upon.

Where should we look for innovations that will influence the design

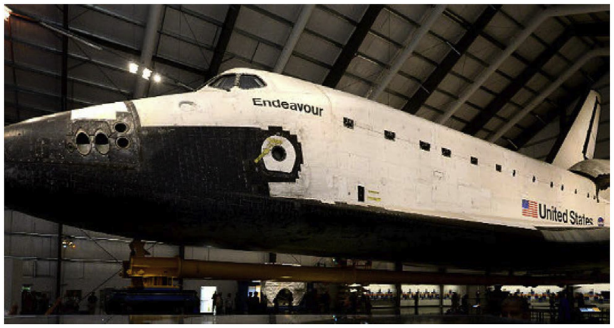

Fig. 11. The Space Shuttle Endeavour, the platform that hosted the SIR-C/X-SAR system on both flights in 1994, has retired to its new home at the Los Angeles Science Museum.

of SAR systems over the next 25 years? Speculating that far ahead, we appear to have reached a fork in the road, with three branches. The first branch leads to multi-mode systems utilizing phased array technology in relatively complex, adaptive systems like Sentinel-1, ALOS-2, Radarsat RCM, NISAR, and Tandem-L, flying on a handful of fairly large, dedicated platforms (Moreira et al., 2013). Innovation along this branch will be through the application of sophisticated modes of operation such as SweepSAR, TOPSAR, ATI, PolInSAR and Tomography. Most of these systems have embraced the mow-the-lawn paradigm, and the resulting systematic acquisition of huge volumes of SAR data will surely overwhelm scientists without the application of machine learning and data analytics to efficiently extract information in a timely fashion. The second branch heads off towards simpler systems that embrace the Smallsat paradigm, each with reduced capability, that can be deployed in constellations of 10 or more to deliver increased temporal revisit frequency, or multi-static imaging capability. Innovation along this branch will be through miniaturization of radar electronics, and the mechanical design of antennas that can be stowed in very small volumes. As Smallsat SAR constellations grow large enough, and capable enough, leading to increased data volumes, machine learning and data analytics will have a role to play there too. The third branch points in the direction of Signals-of-Opportunity systems receiving signals from a multitude of RF sources in orbit, that fit on very small satellites, and can be deployed as constellations in very large numbers. Innovation here will be an endeavor to see how much information can be squeezed out of this unconventional approach to remote sensing, and whether the rich variety of techniques developed for monostatic SAR systems (as described in this paper) can be adapted to this type of bistatic measurement. These three innovation branches are not mutually exclusive – they can all co-exist, since there will likely be relatively little overlap in the science and applications they address, each serving different purposes. Further, Medium Earth Orbits (MEO) and Geosynchronous Earth Orbits (GEO) can be exploited in order to achieve an optimum system concept and design in terms of coverage, geometric resolution and number of satellites.

The elements that made the SIR-C/X-SAR mission a success are now scattered to the four winds: the huge SAR antennas and the radar electronics are in storage, the Space Shuttle Endeavour found a home at the Los Angeles Science Museum (Fig. 11), and the scientists and engineers who worked on the project have long since moved on to new pastures. But the most important piece of the system lives on – the data, which are still accessible through the long-term archive at the U.S. Geological Survey (USGS)'s Earth Resources Observation and Science (EROS) Center (USGS, 2019) and at DLR's Earth Observation Center (DLR, 2019). (Meyer et al., 2017) have outlined a plan for a new SIR-C/X-SAR data processor being developed at the Alaska Satellite Facility in Fairbanks, and it would be timely to see this realized on the occasion of the 25-year anniversary of the missions. It might make an interesting application of machine learning and data analytics to compare data from today's spaceborne SARs with the original, reprocessed SIR-C/X-SAR data and look for differences between that represent real surface changes over a quarter century.

Acknowledgments

This article is dedicated to our departed colleague Rolando Jordan, who was the lead radar systems engineer for SI-—C, and is missed by all of us. The authors would also like to express their special appreciation for the efforts of Charles Elachi at JPL and Herwig Öttl at DLR, for their vision in conceiving SIR-C/X-SAR as a joint venture, and a follow-on to the earlier Shuttle radars. We would also like to acknowledge the excellent work done by the many scientists who have used SIR-C/X-SAR data in their research, and the many engineers who labored to deliver the success of both missions in 1994. Part of the work described in this paper was carried out at the Jet Propulsion Laboratory, California Institute of Technology, under a contract with the National Aeronautics and Space Administration. Support for the German Aerospace Center was provided by the German government.

References

Abdelsalam, M.G., Stern, R.J., 1996. Mapping Precambrian structures in the Sahara Desert with SIR-C/X-SAR radar: the Neoproterozoic Keraf Suture, NE Sudan. JGR Planets 101 (E10), 23063–23076. https://doi.org/10.1029/96JE01391.

Ahmed, S., Parashar, S., Langham, E., McNally, J., 1993. RADARSAT mission requirements and concept. Can. J. Remote. Sens. 19 (4).

Ainsworth, T.L., Schuler, D.S., Lee, J.-S., 2008. Polarimetric SAR characterization of man-made structures in urban areas using normalized circular-pol correlation coefficients. Remote Sens. Environ. 112, 2876–2885.

Albright, T.P., et al., 1998. Classification of surface types using SIR-C/X-SAR, Mount Everest Area, Tibet. JGR Planets 103 (E11), 25823–25837. https://doi.org/10.1029/98JE01893.

Alsdorf, D.E., Smith, L.C., Melack, J.M., 2001. Amazon floodplain water level changes measured with interferometric SIR-C radar. IEEE Trans. Geosci. Remote Sensing 39 (2), 423–431.

Attema, E., Desnos, Y.-L., Duchossois, G., 2000. Synthetic aperture radar in Europe: ERS, Envisat and beyond. Johns Hopkins APL Technical Digest 21 (1).

Bamler, R., 1995. Optimum look weighting for burst-mode and ScanSAR processing. IEEE Trans. Geosci. Remote Sens. 33 (3), 722–725.

Beal, R.C., Monaldo, F.M., 1995. Real-time observations of southern ocean wave fields form the shuttle imaging radar. IEEE Trans. on Geoscience and Remote Sensing 33 (4), 942–949.

Beal, R.C., Oden, S.F., McArthur, J.L., 1991. A real-time SAR processor for ocean wave spectra. In: Proc. IGARSS 1991, Espoo, Helsinki, Finland.

Bergen, K.M., et al., 1998. Characterizing carbon in a northern forest by using SIR-C/X-SAR imagery. Remote Sens. Environ. 63 (1), 24–39. https://doi.org/10.1016/S0034-4257(97)00103-X.

Bird, R., Whittaker, P., Stern, B., Angli, N., Cohen, M., Guida, R., 2013. NovaSAR-S: A low cost approach to SAR applications. In: Conference Proceedings of 2013 Asia-Pacific Conference on Synthetic Aperture Radar (APSAR), pp. 84–87.

Blackmore, L., et al., 2011. Instrument pointing capabilities: past, present and future. In: AAS Guidance and Control Conference, Breckenridge, Colorado.

Boerner, W.M., et al., 1988. Direct and inverse methods in radar polarimetry. In: Proc. of NATO Advanced Research Workshop, Bad Windsheim, 18–24 Sept 1988.

Boerner, W. M., et al. (Eds.), 1992. Direct and inverse methods in radar polarimetry, published in book form as: NATO–ASI Series C: Math and Phys. Sciences, Vol C-350, Parts 1 and 2, D. Reidel Publ. Co., Kluwer Aademic Publ., Dordrecht, Netherlands, 1992.

Boerner, W.M., Mott, H., Lüneburg, E., Livingstone, C., Brisco, B., Brown, R., Paterson, J.S., 1998. Polarimetry in Radar Remote Sensing: Basic and Applied Concepts, Principles and Applications of Imaging Radar: Manual of Remote Sensing, Third edition. vol. 2. pp. 271–357.

Bueso-Bello, J.L., et al., 2017. Performance analysis of TanDEM-X quad-polarization products in pursuit monostatic mode. IEEE J. Sel. Topics Appl. Earth Observ. Remote Sens 10 (5), 1853–1869.

Campbell, B.A., Freeman, A., Veilleux, L., Huneycutt, B., Jones, M., Shotwell, R., 2004. A P-band radar mission to Mars. In: Proc. IEEE Aerospace Conference, Big Sky, MT.

Campbell, B.A., Maxwell, T., Freeman, A., 2004a. Mars orbital SAR: obtaining geologic information from radar polarimetry. J. Geophys. Res. 109. https://doi.org/10.1029/2004JE002264.

Capella Space, 2019. https://www.capellaspace.com, Accessed date: 22 March 2019.

Chang, C.Y., Curlander, J.C., 1992. Application of the multiple PRF technique to resolve Doppler centroid estimation ambiguity for spaceborne SAR. IEEE Trans. on Geoscience and Remote Sensing 30 (5), 941–949. https://doi.org/10.1109/36.175329.

Chang, C.Y., Jin, M.Y., Lou, Y.-L., Holt, B., 1995. First SIR-C ScanSAR results. IEEE Trans. on Geoscience and Remote Sensing 34 (5), 1278–1281.

Charbonneau, F.J., et al., 2010. Compact polarimetry overview and applications

assessment. Can. J. Remote. Sens. 36 (sup 2), S298–S315.
Chen, F., Lasaponara, R., Masini, M., 2015. An overview of satellite synthetic aperture radar remote sensing in archaeology: from site detection to monitoring. J. Cult. Herit. https://doi.org/10.1016/j.culher.2015.05.003.
Cimino, J., Elachi, C., Settle, M., 1986. SIR-B—the 2nd shuttle imaging radar experiment. IEEE Trans. Geosci. Remote Sens. 24 (4), 445–452.
Cloude, S.R., Papathanassiou, K.P., 1998. Polarimetric SAR interferometry. IEEE Trans. on Geoscience and Remote Sensing 36 (5), 1551–1565.
Cloude, S., Pottier, E., 1996. A review of target decomposition algorithms in radar polarimetry. IEEE Trans. on Geoscience and Remote Sensing 34 (2), 498–518.
Cloude, S.R., Corr, D.G., Williams, M.L., 2003. Target detection beneath foliage using polarimetric synthetic aperture radar interferometry. Waves in Random Media 2, S393–S414. https://doi.org/10.1088/0959-7174/14/2/015.
Cohen, M., et al., 2017. NovaSAR-S Low Cost Spaceborne SAR Payload Design, Development and Deployment of a New Benchmark in Spaceborne Radar, IEEE Radar Conference, Seattle, WA.
Coltelli, M., et al., 1996. SIR-C/X-SAR multifrequency multipass interferometry: a new tool for geological interpretation. JGR 101 (E10), 23,127–23,148.
Dabbagh, A.E., Al-Hinai, K.G., Khan, M.A., 1997. Detection of sand-covered geologic features in the Arabian Peninsula using SIR-C/X-SAR data. Remote Sens. Environ. 59 (2), 375–382. https://doi.org/10.1016/S0034-4257(96)00160-5.
Danklmayer, A., Doring, B.J., Schwerdt, M., Chandra, M., 2009. Assessment of atmospheric propagation effects in SAR images. IEEE Trans. Geosci. Remote Sens. 47 (10), 3507–3518.
Desnos, Y.-L., et al., 2000. ASAR – Envisat's advanced synthetic aperture radar. ESA Bull. 102.
Di Lazzaro, M., Angino, G., Piemontese, M., Capuzi, A., Leonardi, R., 2008. COSMO-SkyMed: the dual-use component of a geospatial system for environment and security. In: Proceedings of the 2008 IEEE Aerospace Conference, Big Sky, MT, USA.
Dieterle, G., Schlude, F., 1982. The European MRSE-project on the first spacelab flight. In: Proc. IGARSS'82. Munich, Germany.
DLR, 2019. X-SAR data archive. https://geoservice.dlr.de/egp/, Accessed date: 22 March 2019.
Dobson, M.C., Ulaby, F.T., Pierce, L.E., Sharik, T.L., Bergen, K.M., Kellndorfer, J., ... Sarabandi, K., 1995. Estimation of forest biophysical characteristics in Northern Michigan with SIR-C/X-SAR. IEEE Trans. Geosci. Remote Sens. 33 (4), 877–895.
Dubois, P.C., van Zyl, J.J., Engman, T., 1995. Measuring soil moisture with imaging radars. IEEE Trans. on Geoscience and Remote Sensing 33 (4), 915–926.
Elachi, C., Brown, W.E., Cimino, J.B., Dixon, T., Evans, D.L., Ford, J.P., et al., 1982. Shuttle imaging radar experiment. Science 218, 996–1004.
eoportal, 2019. RISAT-2 (radar imaging Satellite-2). https://earth.esa.int/web/eoportal/satellite-missions/r/risat-2, Accessed date: 22 March 2019.
eoportal, 2019a. PAZ SAR satellite mission of Spain. https://directory.eoportal.org/web/eoportal/satellite-missions/p/paz, Accessed date: 22 March 2019.
eoportal, 2019b. NISAR (NASA-ISRO synthetic aperture radar) mission. https://directory.eoportal.org/web/eoportal/satellite-missions/n/nisar, Accessed date: 27 May 2019.
Evans, D.L., 2006. Spaceborne imaging radar-C/X-band synthetic aperture radar (SIR-C/X-SAR): a look back on the tenth anniversary. IEE Proceedings - Radar, Sonar and Navigation 153 (2), 81–85. https://doi.org/10.1049/ip-rsn:20045095.
Evans, D.L., Plaut, J.J., Stofan, E.R., 1997. Overview of the spaceborne imaging radar-C/X-band synthetic aperture radar (SIR-C/X-SAR) missions. Remote Sens. Environ. 59 (2), 135–140. https://doi.org/10.1016/S0034-4257(96)00152-6.
Evans, D.E., et al., 2005. Seasat—a 25-year legacy of success. Remote Sens. Environ. 94, 384–404.
Fang, Y., Moore, R.K., 1997. Inflight vertical antenna patterns for SIR-C from Amazon rain-forest observations. Remote Sens. Environ. 59 (2), 407–414. https://doi.org/10.1016/S0034-4257(96)00163-0.
Farr, T.G., Kobrick, M., 2000. The shuttle radar topography mission. EOS Trans. Am. Geophys. Union 81 (48), 583–585. https://doi.org/10.1029/EO081i048p00583.
Farr, Tom G., Rosen, Paul A., Caro, Edward, Crippen, Robert, Duren, Riley, Hensley, Scott, Kobrick, Michael, Paller, Mimi, Rodriguez, Ernesto, Roth, Ladislav, Seal, David, Shaffer, Scott, Shimada, Joanne, Umland, Jeffrey, Werner, Marian, Oskin, Michael, Burbank, Douglas, Alsdorf, Douglas, 2007. The shuttle radar topography mission. Rev. Geophys. 45 (2), RG2004.
Ferrazzoli, P., et al., 1997. The potential of multifrequency polarimetric SAR in assessing agricultural and arboreous biomass. IEEE Trans. Geosci. Remote Sensing (1), 5–17. https://doi.org/10.1109/36.551929.
Filippazzo, G., Dinand, S., 2017. The potential impact of small satellite radar constellations on traditional space system. In: 5th Federated and Fractionated Satellite Systems Workshop. ISAE SUPAERO, Toulouse, France.
Floricioiu, D., Rott, H., 2001. Seasonal and short-term variability of multifrequency, polarimetric radar backscatter of Alpine terrain from SIR-C/X-SAR and AIRSAR data. IEEE Trans. Geosci. Remote Sens. 39 (12), 2634–2648. https://doi.org/10.1109/36.974998.
Foody, g.M., et al., 1997. Observations on the relationship between SIR-C radar backscatter and the biomass of regenerating tropical forests. Int. J. Remote Sens. 18 (3), 687–694. https://doi.org/10.1080/014311697219024.
Fornaro, G., et al., 2012. SAR tomography: an advanced tool for 4D spaceborne radar scanning with application to imaging and monitoring of cities and single buildings. IEEE Geoscience and Remote Sensing Society Newsletter 9–17.
Forster, R.R., Isacks, B.L., Das, S.B., 1996. Shuttle imaging radar (SIR-C/X-SAR) reveals near-surface properties of the South Patagonian Icefield. JGR Planets 101 (E10), 23169–23180. https://doi.org/10.1029/96JE01950.
Fox, P., Luscombe, A.P., Ali, Z., 2002. The Radarsat-2 Mission, New Modes and Techniques, Proceedings of IAC (International Astronautical Congress), Houston, Tx.
Freeman, A., 2004. Calibration of linearly polarized polarimetric SAR data subject to Faraday rotation. IEEE Trans. Geosci. Remote Sens. 42 (8), 1617–1624.
Freeman, A., 2009. On the Design of Spaceborne Polarimetric SARs. In: Proc. Radarcon '09, Pasadena, CA.
Freeman, A., 2018. Design Principles for Smallsat SARs. SSC18-V-01, Smallsat Conference, Logan Utah.
Freeman, A., Chahat, N., 2017. S-Band Smallsat InSAR constellation for surface deformation science. Radar Conference (RadarCon), May 2017 IEEE 0867–0872.
Freeman, A., Durden, S., 1998. A three-component scattering model for polarimetric SAR data. IEEE Trans. on Geoscience and Remote Sensing 36 (3), 963–973.
Freeman, A., Saatchi, S., 2004. On the detection of Faraday rotation in linearly polarized, L-band SAR backscatter signatures. IEEE Trans. Geosci. Remote Sens. 42 (8), 1607–1616.
Freeman, A., Smrekar, S., 2015. VERITAS – a discovery-class Venus surface geology and geophysics mission. In: 11th Low Cost Planetary Missions Conference, Berlin, Germany.
Freeman, A., Durden, S.D., Zimmermann, R., 1992. Mapping Sub-tropical Vegetation Using Multi-frequency Multi-polarization SAR Data, Proc. IGARSS '92, Houston Texas.
Freeman, A., Cruz, J., Alves, M., Chapman, B., Shaffer, S., Turner, E., 1994. SIR-C Calibration Results, in Proc. IGARSS '94, Pasadena, California.
Freeman, A., Cruz, J., Alves, M., Chapman, B., Shaffer, S., Turner, E., 1995. SIR-C data quality and calibration results. IEEE Trans. on Geoscience and Remote Sensing 33 (4), 848–857.
Freeman, A., E. Caro, R. Jordan, Y. Kim, J. Klein, Y. Lou, Y. Shen, S Shaffer, C.Y. Chang and F. Stuhr, 1996. Lessons learned from the first two SIR-C missions - an engineering perspective, Proc. EUSAR '96, Königswinter, Germany, 37–40.
Freeman, A., Johnson, W.T.K., Honeycutt, B., Jordan, R., Hensley, S., Siqueira, P., Curlander, J., 2000. The myth of the minimum SAR antenna area constraint. IEEE Trans. Geosci. Remote Sensing 38, 320–324.
Freeman, A., Pi, X., Chapman, B., 2009. Calibration of PalSAR polarimetric data. In: Proc. PolinSAR, (Frascati, Italy).
Freeman, A., Krieger, G., Rosen, P., Younis, M., Johnson, W.T.K., Huber, S., Jordan, R., Moreira, A., 2009a. SweepSAR: Beam-forming on Receive Using a Reflector-Phased Array Feed Combination for Spaceborne SAR, Proc. Radarcon '09, Pasadena, CA.
Freeman, A., Pi, X., Heggy, E., 2017. Radar sounding through the Earth's ionosphere at 45 MHz. IEEE Trans. Geosci. Remote Sens. 55 (10), 5833–5842. https://doi.org/10.1109/TGRS.2017.2715838.
Frulla, L., et al., 2011. SAOCOM Mission Overview, 2011 CEOS SAR Calibration and Validation Workshop Fairbanks, AK.
Fujita, M., et al., 1998. Polarimetric calibration of the SIR-C C-band channel using active radar calibrators and polarization selective dihedrals. IEEE Trans. on Geoscience and Remote Sensing 36 (6), 1872–1878. https://doi.org/10.1109/36.729358.
Gabele, M., Brautigam, B., Schulze, D., Steinbrecher, U., Tous-Ramon, N., Younis, M., 2009. Fore and aft channel reconstruction in the TerraSAR-X dual receive antenna mode. IEEE Trans. Geosci. Remote Sens. 48 (2), 795–806.
Gade, M., Alpers, W., Huhnerfuss, H., Masuko, H., Kobayashi, T., 1998. Imaging of biogenic and anthropogenic ocean surface films by the multifrequency/multipolarization SIR-C/X-SAR. JGR Oceans 103 (C9). https://doi.org/10.1029/97JC01915.
Galvez, R., Gaylor, S., Young, C., Patrick, N., Johnson, D., Ruiz, J., 2019. The space shuttle and its operations. https://www.nasa.gov/centers/johnson/pdf/584722main_Wings-ch3a-pgs53-73.pdf, Accessed date: 25 March 2019.
Gebert, N., Krieger, G., Moreira, A., 2009. Digital beamforming on receive: techniques and optimization strategies for high-resolution wide-swath SAR imaging. IEEE Trans. Aerosp. Electron. Syst. 45 (2), 564–592.
Geudtner, D., Zink, M., Gierull, C., Shaffer, S., 2002. Interferometric alignment of the X-SAR antenna system on the space shuttle radar topography mission. IEEE Trans. on Geoscience and Remote Sensing 40 (5), 995–1006.
Greeley, R., Blumberg, D., 1995. Preliminary analysis of shuttle radar lab (SRL-1) data to study aeolian features and processes. IEEE Trans. on Geoscience and Remote Sensing 33 (4), 927–933.
Gunter's Space Page, 1964. Quill (P-40). https://space.skyrocket.de/doc_sdat/quill.htm, Accessed date: 21 March 2019.
Guo, H., et al., 1996. Detection of structural and lithological features underneath a vegetation canopy using SIR-C/X-SAR data in Zhao Qing test site of southern China. JGR Planets 101 (E10), 23101–23108. https://doi.org/10.1029/96JE01974.
Harrell, P.A., Kasischke, E.S., Bourgeau-Chavez, L.L., Haney, E.M., Christensen, N.L., 1997. Evaluation of approaches to estimating aboveground biomass in Southern pine forests using SIR-C data. Remote Sens. Environ. 59 (2), 223–233. https://doi.org/10.1016/S0034-4257(96)00155-1.
Hensley, S., Smrekar, S., Shaffer, S., Paller, M., Figueroa, H., Freeman, A., Hodges, R., Walkemeyer, P., 2015. VISAR: A Next Generation Interferometric Radar for Venus Exploration, Venus Lab and Technology Workshop, Houston, TX.
Hess, L.L., Melack, J.M., 2003. Remote sensing of vegetation and flooding on Magela Creek Floodplain (Northern Territory, Australia) with the SIR-C synthetic aperture radar. Hydrobiologia 500, 65–82. https://doi.org/10.1023/A:1024665017985.
Hess, L.L., Melack, J.M., Filoso, S., Wang, Y., 1995. Delineation of inundated area and vegetation along the Amazon floodplain with the SIR-C synthetic aperture radar. IEEE Trans. on Geoscience and Remote Sensing 33 (4), 896–904.
Holt, B., 1998. Introduction to special section: studies of the ocean surface from the spaceborne imaging radar-C/X-band SAR experiments. Journal of Geophysical Research: Oceans 103 (C9). https://doi.org/10.1029/98JC01618.
Huadong, G., Jingjuan, L., Changlin, W., Chao, W., Farr, T.G., Evans, D.L., 1997. Use of multifrequency, multipolarization shuttle imaging radar for volcano mapping in the Kunlun Mountains of Western China. Remote Sens. Environ. 59 (2), 364–374. https://doi.org/10.1016/S0034-4257(96)00175-7.

Iceye, 2019. Iceye Global Satellite Monitoring. https://www.iceye.com, Accessed date: 22 March 2019.
Ishimaru, A., Kuga, Y., Liu, J., Kim, Y., Freeman, A., 1999. Ionospheric effects on synthetic aperture radar at 100 MHz to 2 GHz. Radio Sci. 34 (1), 257–268.
Jameson, A.R., Li, F.K., Durden, S.L., Haddad, Z.S., Holt, B., Fogarty, T., Im, E., Moore, R.K., 1997. SIR-C/X-SAR observations of rain storms. Remote Sens. Environ. 59 (2), 267–279. https://doi.org/10.1016/S0034-4257(96)00159-9.
Jezek, K.C., 2008. The RadarSAT-1 Antarctic mapping project. Byrd Polar Research Center(0896-2472)(22) Report No.. ISSN:.
Jezek, K.C., Curlander, J., Norikane, L., Carsey, F., Crawford, J., Wales, C., Muller, J., 1996. RADARSAT: The Antarctic Mapping Project. Geoscience and Remote Sensing Symposium Proceedings. IGARSS '96 3. pp. 1775–1776.
Jordan, R.L., Huneycutt, B.L., Werner, M., 1995. The SIR-C/X-SAR synthetic aperture radar system. IEEE Trans. on Geoscience and Remote Sensing 33 (4), 829–839.
JPL, 2019. NASA-ISRO SAR Mission (NISAR). https://nisar.jpl.nasa.gov/ (accessed 22 March 2019).
Kasischke, E. S. Melack, J. M. and Dobson, M. C. 1997. The use of imaging radars for ecological applications, a review Remote Sens. Environ., 59, 2, 141-156, DOI: 10.1016/S0034-4257(96)00148-4.
Kim, J.S., Papathanassiou, K.P., Sato, H., Quegan, S., 2017. Detection and estimation of equatorial spread F scintillations using synthetic aperture radar. IEEE Trans. Geosci. Remote Sens. 55 (12), 6713–6725.
Klein, J.D., 1992. Calibration of complex polarimetric SAR imagery using backscatter correlations. IEEE Trans. Aerosp. Electron. Syst. 28 (1), 183–194.
Krieger, G., Moreira, A., Hajnsek, I., Werner, M., Fiedler, H., Settelmeyer, E., 2005. The TanDEM-X Mission Proposal, Proceedings of the ISPRS Hannover Workshop 2005, Hannover, Germany.
Krieger, G., Moreira, A., Fiedler, H., Hajnsek, I., Werner, M., Younis, M., Zink, M., 2007. TanDEM-X: a satellite formation for high resolution SAR interferometry. IEEE Trans. Geosci. Remote Sens. 45 (11), 3317–3341.
Krieger, G., Hajnsek, Irena, Papathanassiou, Konstantinos, Eineder, Michael, Younis, Marwan, Zan, Francesco De, Huber, Sigurd, Lopez-Dekker, Paco, Prats, Pau, Werner, Marian, Shen, Yuhsyen, Freeman, Anthony, Rosen, Paul, Hensley, Scott, Johnson, W., Veilleux, Louise, Grafmueller, Bernhard, Werninghaus, Rolf, Bamler, Richard, Moreira, Alberto, 2010. Tandem-L: An Innovative Interferometric and Polarimetric SAR Mission to Monitor Earth System Dynamics With High Resolution, IGARSS 2010, Hawaii. pp. 253–256.
Kruse, F., 1996. Geologic Mapping Using Combined Analysis of Airborne Visible/Infrared Imaging Spectrometer (AVIRIS) and SIR-C/X-SAR Data, Proc. SPIE 2819, Imaging Spectrometry II. https://doi.org/10.1117/12.258078.
Kusky, T.M., Ramadan, T.M., 2002. Structural controls on Neoproterozoic mineralization in the South Eastern Desert, Egypt: an integrated field, Landsat TM, and SIR-C/X SAR approach. J. Afr. Earth Sci. 35 (1), 107–121. https://doi.org/10.1016/S0899-5362(02)00029-5.
Lanari, R., et al., 1996. Generation of digital elevation models by using SIR-C/X-SAR multifrequency two-pass interferometry: the Etna case study. IEEE Trans. on Geoscience and remote Sensing 34 (5), 1097–1114. https://doi.org/10.1109/36.536526.
Lanari, R., Tesauro, M., Sansosti, E., Fornaro, G., 2001. Spotlight SAR data focusing based on a two-step processing approach. IEEE Trans. on Geoscience and Remote Sensing 39 (9), 1993–2004.
Le Toan, T., et al., 2011. The BIOMASS mission: mapping global forest biomass to better understand the terrestrial carbon cycle. Remote Sens. Environ. 115 (11), 2850–2860.
Lee, S.-R., 2010. Overview of KOMPSAT-5 Program, Mission, and System, Proceedings of IGARSS (IEEE International Geoscience and Remote Sensing Symposium) 2010, Honolulu, HI, USA.
Lee, J.-S., et al., 2000. A new technique for noise filtering of SAR interferometric phase images. IEEE Trans. on Geoscience and remote Sensing 36 (5), 1456–1465. https://doi.org/10.1109/36.718849.
Li, F.K., Held, D.N., Curlander, J.C., Wu, C., 1985. Doppler parameter estimation for spaceborne synthetic-aperture radars. IEEE Trans. Geosci. Remote Sens. (1), 47–56.
Li, X.W., Guo, H.D., Wang, C.L., Li, Z., Liao, J.J., 2003. DEM generation in the densely vegetated area of Hotan, north-west China using SIR-C repeat pass polarimetric SAR interferometry. Int. J. Remote Sens. (14), 2997–3003. https://doi.org/10.1080/0143116031000094773.
Liu, J., Kuga, Y., Ishimaru, A., Pi, X., Freeman, A., 2003. Ionospheric effects on SAR imaging: a numerical study. IEEE Trans. Geosci. Remote Sens. 41 (5), 939–947. https://doi.org/10.1109/TGRS.2003.811813. Part 1.
Lowe, S.T., LaBrecque, J.T., Zuffada, C., Romans, L.J., Young, L.E., Hajj, G.A., 2002. First spaceborne observation of an Earth-reflected GPS signal. Radio Sci. 37 (1).
Macelloni, G., et al., 1999. The SIR-C/X-SAR experiment on Montespertoli: sensitivity to hydrological parameters. Int. J. Remote Sens. 20 (13), 2597–2612. https://doi.org/10.1080/014311699211958.
MacKay, M.E., Mouginis-Mark, P.J., 1997. The effect of varying acquisition parameters on the interpretation of SIR-C radar data: the Virunga volcanic chain. Remote Sens. Environ. 59 (2), 321–336. https://doi.org/10.1016/S0034-4257(96)00144-7.
MacKay, M., Rowland, S., Mouginis-Mark, P., et al., 1998. Thick lava flows of Karisimbi Volcano, Rwanda; insights from SIR-C interferometric topography. Bull. Volcanol. 60, 239–251. https://doi.org/10.1007/s004450050230.
Macklin, J.T., Stapleton, N.R., 1998. Radar backscatter statistics from the sea surface: implications of SIR-C/X-SAR observations from the NE Atlantic. Journal of Geophysical Research: Oceans 103 (C9). https://doi.org/10.1029/97JC03423.
Madsen, S.N., 1989. Estimating the Doppler centroid of SAR data. IEEE Trans. Aerosp. Electron. Syst. 25 (2), 134–140.
Mango, S., et al., 1995. Remote Sensing of Current-Wave Interactions With SIR-C/X-SAR During SRL-1 and SRL-2 at the Gulf Stream Supersite, Proc. IGARSS '95, Florence, Italy.
Masuko, H., Kobayashi, T., Okamoto, K.-I., Alpers, W., 1995. Observation of Artificial Slicks With SIR-C/X-SAR Around Japan, Proceedings of IGARSS '95, Firenze, Italy. https://doi.org/10.1109/IGARSS.1995.520244.
Matzler, C., Strozzi, T., Weise, T., Floricioiu, D.-M., Rott, H., 1997. Microwave snowpack studies made in the Austrian Alps during the SIR-C/X-SAR experiment. Int. J. Remote Sens. 18 (12), 2505–2530. https://doi.org/10.1080/014311697217440.
Mchone, J.F., et al., 2002. Space shuttle observations of terrestrial impact structures using SIR-C and X-SAR radars. Meteorit. Planet. Sci. 37 (3), 407–420. https://doi.org/10.1111/j.1945-5100.2002.tb00824.x.
Meadows, P., 1994. ERS-1 SAR Analogue to Digital Convertor Saturation, CEOS SAR Calibration Workshop, Ann Arbor Michigan.
Melsheimer, C., Alpers, W., Gade, M., 1998. Investigation of multifrequency/multi-polarization radar signatures of rain cells over the ocean using SIR-C/X-SAR data. Journal of Geophysical Research: Oceans 103 (C9). https://doi.org/10.1029/98JC00779.
Meyer, F.J., Nicoll, J.B., 2008. Prediction, detection, and correction of faraday rotation in full-polarimetric L-band SAR data. IEEE Trans. Geosci. Remote Sens. 46 (10), 3076–3086.
Meyer, F. J., V. Gracheva, Zeivogel, S., Arko, S. A., J. Nicol, Rosen, P. A., 2017. Development and validation of a new processor for the SIR—C mission, Proceedings of CEOS SAR Cal/Val Workshop, JPL, Pasadena, CA.
Migliaccio, M., Gambardella, A., Tranfaglia, M., 2007. SAR polarimetry to observe oil spills. IEEE Trans. on Geoscience and remote Sensing 45 (2), 506–511. https://doi.org/10.1109/TGRS.2006.888097.
Misra, T., Rana, S.S., Bora, V.H., Desai, N.M., Rao, C.V.N., Rajeevjyothi, N., 2006. SAR Payload of Radar Imaging Satellite (RISAT) of ISRO, Proceedings of EUSAR 2006, Dresden, Germany.
Mittermayer, J., Wollstadt, S., Prats, P., Scheiber, R., 2014. The TerraSAR-X staring spotlight mode concept. IEEE Trans. Geosci. Remote Sens. 52 (6), 3695–3706.
Monaldo, F., Beal, R.C., 1998. Comparison of SIR-C SAR wavenumber spectra with WAM model predictions. Journal of Geophysical Research: Oceans 103 (C9). https://doi.org/10.1029/98JC01457.
Moore, R.K., Claassen, J.P., Lin, Y.H., 1981. Scanning spaceborne synthetic aperture radar with integrated radiometer. IEEE Trans. Aerosp. Electron. Syst. (3), 410–421.
Moore, R.K., Mogili, A., Fang, Y., Beh, B., Ahamad, A., 1997. Rain measurement with SIR-C/X-SAR. Remote Sens. Environ. 59 (2), 280–293. https://doi.org/10.1016/S0034-4257(96)00147-2.
Moore, E., Freeman, A., Hensley, S., 2006. Spaceborne and airborne radar at Angkor: introducing new technology to the ancient site. In: Wiseman, J., El-Baz, F. (Eds.), Remote Sensing in Archaeology. Interdisciplinary Contributions to Archaeology. Springer, New York, NY. https://doi.org/10.1007/0-387-44455-6_8.
Moreira, A., 1992. Real-time synthetic aperture radar (SAR) processing with a new sub-aperture approach. IEEE Trans. on Geoscience and Remote Sensing 30 (4), 714–722. https://doi.org/10.1109/36.158865.
Moreira, J., et al., 1995. X-SAR interferometry: first results. IEEE Trans. on Geoscience and Remote Sensing 33 (4), 950–956.
Moreira, A., Krieger, G., Hajnsek, I., Hounam, D., Werner, M., Riegger, S., Settelmeyer, E., 2004. TanDEM-X: a TerraSAR-X add-on satellite for single-pass SAR interferometry. In: IEEE International Geoscience and Remote Sensing Symposium (IGARSS). Vol. 2. pp. 1000–1003.
Moreira, A., Prats-Iraola, P., Younis, M., Krieger, G., Hajnsek, I., Papathanassiou, K.P., 2013. A tutorial on synthetic aperture radar. IEEE Geoscience and Remote Sensing Magazine 1 (1), 6–43.
Moreira, A., Krieger, G., Hajnsek, I., Papathanassiou, K., Younis, M., Lopez-Dekker, F., Huber, S., Villano, M., Pardini, M., Eineder, M., De Zan, F., Parizzi, A., 2015. Tandem-L: a highly innovative bistatic SAR mission for global observation of dynamic processes on the Earth's surface. IEEE Geoscience and Remote Sensing Magazine (GRSM) 3 (2), 8–23.
Mouginis-Mark, P.J., 1995. Preliminary observations of volcanoes with the SIR-C radar. IEEE Trans. on Geoscience and Remote Sensing 33 (4), 934–941.
Nagai, T., Yamaguchi, Y., Yamada, H., 1997. Use of multi-polarimetric enhanced images in SIR-C/X-SAR land-cover classification. IEICE Trans. Commun. E80-B (11), 1696–1702.
Nannini, M., Martone, M., Rizzoli, P., Prats-Iraola, P., Rodriguez-Cassola, M., Reigber, A., Moreira, A., 2019. Coherence-based SAR tomography for spaceborne applications. Remote Sens. Environ. 225, 107–114.
Narayanan, R., Hirsave, P.P., 2001. Soil moisture estimation models using SIR-C SAR data: a case study in New Hampshire, USA. Remote Sens. Environ. 75 (3), 385–396. https://doi.org/10.1016/S0034-4257(00)00181-4.
Nomoko, Y., et al., 1991. Japanese Earth resources Satellite-1 synthetic aperture radar. Proc. IEEE 79 (6).
Öttl, H., 1997. The SIR-C/X-SAR missions — overview and some results. Acta Astronautica 41 (3), 155–163.
Paloscia, S., 2002. A summary of experimental results to assess the contribution of SAR for mapping vegetation biomass and soil moisture. Can. J. Remote. Sens. (2), 246–261. https://doi.org/10.5589/m02-020.
Pierce, l.E., et al., 1994. Knowledge-based classification of polarimetric SAR images. IEEE Trans. on Geoscience and remote Sensing 32 (5), 1081–1086. https://doi.org/10.1109/36.312896.
Pierce, l.E., et al., 1998. Multitemporal land-cover classification using SIR-C/X-SAR imagery. Remote Sens. Environ. 64 (1), 20–33. https://doi.org/10.1016/S0034-4257(97)00165-X.
Ponte, S., Vetrella, S., 1997. The SIR-C/X-SAR Italian experiments at Matera: instrumentation and measurement results. Remote Sens. Environ. 59 (2), 397–406. https://doi.org/10.1016/S0034-4257(96)00162-9.

Pope, K.O., Rejmankova, E., Paris, J.F., Woodruff, R., 1997. Detecting seasonal flooding cycles in marshes of the Yucatan Peninsula with SIR-C polarimetric radar imagery. Remote Sens. Environ. 59 (2), 157–166. https://doi.org/10.1016/S0034-4257(96)00151-4.

Pope, K.O., Rejmankova, E., Paris, J.F., 2001. Spaceborne imaging radar-C (SIR-C) observations of groundwater discharge and wetlands associated with the Chicxulub impact crater, northwestern Yucatan Peninsula. Mexico. Geol. Soc. Am. Bull. 3, 403–416. https://doi.org/10.1130/0016-7606(2001)113<0403:SIRCSC>2.0.CO;2.

Potin, P., Rosich, B., Grimont, P., Miranda, N., Shurmer, I., O'Connell, A., Krassenburg, M., 2016. Sentinel-1 mission status. In: Proceedings of EUSAR 2016: 11th European Conference on Synthetic Aperture Radar, pp. 1–6.

Pultz, T.J., Crevier, Y., Brown, R.J., Boisvert, J., 1997. Monitoring local environmental conditions with SIR-C/X-SAR. Remote Sens. Environ. 59 (2), 248–255. https://doi.org/10.1016/S0034-4257(96)00157-5.

Purdue, 2019. SNoOPI: Purdue CubeSat Project Selected for Flight by NASA.

Quegan, S., Le Toan, T., Chave, J., Dall, J., Exbrayat, J.F., Minh, D.H.T., Lomas, M., D'Alessandro, M.M., Paillou, P., Papathanassiou, K., Rocca, F., Saatchi, S., Scipal, K., Shugart, H., Smallmane, T. L., Soja, M. J., Tebaldinig, S., Ulander, L., Villard, L., and Williams, M., 2019. The European Space Agency BIOMASS mission: measuring forest above-ground biomass from space, Remote Sens. Environ., Vol. 227, pp. 44–60, DOI: https://doi.org/10.1016/j.rse.2019.03.032.

Ramadan, T.M., Abdelsalam, M.G., Stern, R.J., 2001. Mapping gold-bearing massive sulfide deposits in the Neoproterozoic Allaqi Suture, Southeast Egypt with Landsat TM and SIR-C/X SAR images. Photogramm. Eng. Remote Sens. 67 (4) -497. (DOI: 0099-1112/01/6704-491$3.00).

Raney, R.K., Freeman, A., 2009. Hybrid-Polarity SAR Architecture, Proc. PolinSAR 2009, Frascati, Italy.

Ranson, K.J., Sun, G., 1997. An evaluation of AIRSAR and SIR-C/X-SAR images for mapping northern forest attributes in Maine, USA. Remote Sens. Environ. 59 (2), 203–222. https://doi.org/10.1016/S0034-4257(96)00154-X.

Ranson, K.J., Ulaby, F.T., Pierce, L.E., 1995. Boreal forest ecosystem characterization with SIR-C/XSAR. IEEE Trans. on Geoscience and Remote Sensing 33 (4), 867–876.

Ranson, K.J., et al., 2001. Characterization of forests in Western Sayani Mountains, Siberia from SIR-C SAR data. Remote Sens. Environ. 75 (2), 188–200. https://doi.org/10.1016/S0034-4257(00)00166-8.

Rao, Y.S., Meadows, P., Kumar, V., 2016. Evaluation of RISAT—1 compact polarization data for calibration. In: Proc. IEEE IGARSS, pp. 3250–3253.

Reigber, A., Moreira, A., 2000. First demonstration of air-borne SAR tomography using multibaseline L-band data. IEEE Trans. Geosci. Remote Sens. 38 (5), 2142–2152.

Rignot, E., William, A., Salas, W.A., Skole, D.L., 1997. Mapping deforestation and secondary growth in Rondonia, Brazil, using imaging radar and thematic mapper data. Remote Sens. Environ. 59 (2), 167–179. https://doi.org/10.1016/S0034-4257(96)00150-2.

Rizzoli, P., Martone, M., Gonzalez, C., Wecklich, C., Tridon, D.B., Bräutigam, B., Bachmann, M., Schulze, D., Fritz, T., Huber, M., Wessel, B., Krieger, G., Zink, M., Moreira, A., 2017. Generation and performance assessment of the global TanDEM-X digital elevation model. ISPRS J. Photogramm. Remote Sens. 132, 119–139.

Rogers, N.C., Quegan, S., 2014. The accuracy of faraday rotation estimation in satellite synthetic aperture radar images. IEEE Trans. Geosci. Remote Sens. 52 (8), 4799–4807. https://doi.org/10.1109/TGRS.2013.2284635.

Romeiser, R., et al., 2002. Study on concepts for radar interferometry from satellites for ocean (and land) applications (KoRIOLiS). http://www.ifm.uni-hamburg.de/~romeiser/koriolis.htmIn: University of Hamburg Technical Report (April 2002).

Rosen, P.A., Hensley, S., Zebker, H.A., Webb, F.H., Fielding, E.J., 1996. Surface deformation and coherence measurements of Kilauea volcano, Hawaii, from SIR-C radar interferometry. J. Geophys. Res.—Planets 101 (E10), 23109–23125.

Rosen, P., et al., 2000. Synthetic aperture radar interferometry. Proc. IEEE 88 (3), 333–382.

Rosenqvist, A., Shimada, M., Chapman, B., Freeman, A., De Grandi, G.F., Saatchi, S., Rauste, Y., 2000. The global rain forest mapping project - a review. Int. J. Remote Sens. 21 (6&7), 1375–1387.

Rosenqvist, A., Shimada, M., Suzuki, S., Ohgushi, F., Tadono, T., Watanabe, M., Aoki, E., 2014. Operational performance of the ALOS global systematic acquisition strategy and observation plans for ALOS-2 PALSAR-2. Remote Sens. Environ. 155, 3–12.

Ruf, C.S., et al., 2018. A new paradigm in Earth environmental monitoring with the CYGNSS small satellite constellation. Nat. Sci. Rep. 2018 (8), 8782. https://doi.org/10.1038/s41598-018-2712.

Saatchi, S., Vianei Soares, J., Salas Alves, D., 1997. Mapping deforestation and land use in amazon rainforest by using SIR-C imagery. Remote Sens. Environ. 59 (2), 191–202. https://doi.org/10.1016/S0034-4257(96)00153-8.

Saito, H., et al., 2018. Engineering-Model Results of Compact X-Band Synthetic Aperture Radar, 4S Symposium, Sorrento, Italy.

Sarabandi, K., Pierce, L., Dobson, M.C., Ulaby, F.T., Stiles, J., Chiu, T.C., De Roo, R., Hartikka, R., Zambetti, A., Freeman, A., 1995. Polarimetric calibration of SIR-C using point and distributed targets. IEEE Trans. on Geoscience and Remote Sensing 33 (4), 858–866.

Schaber, G., McCauley, J.F., Breed, C., 1997. The use of multifrequency and polarimetric SIR-C/X-SAR data in geologic studies of Bir Safsaf, Egypt. Remote Sens. Environ. 59 (2), 337–363. https://doi.org/10.1016/S0034-4257(96)00143-5.

Schmullius, C.C., Evans, D.L., 1997. Review article synthetic aperture radar (SAR) frequency and polarization requirements for applications in ecology, geology, hydrology, and oceanography: a tabular status quo after SIR-C/X-SAR. Int. J. Remote Sens. 18 (13), 2713–2722. https://doi.org/10.1080/014311697217297.

Séguin, G., 2005. A Canadian constellation of C-band SAR satellites. In: Proceedings of the 56th IAC 2005, Fukuoda, Japan.

Séguin, G., Ahmed, S., 2009. RADARSAT constellation, project objectives and status. In: Proceedings of 2009 IEEE International Geoscience and Remote Sensing Symposium. vol. 2. pp. II–894.

Shah, R., Garrison, P., Freeman, A., 2018. Constellations of CubeSats to exploit signals-of-opportunity for Earth system science. In: Proceedings SPIE Optical Engineering + Applications. CubeSats and NanoSats for Remote Sensing II, vol. 10769 (107690D, San Diego, CA).

Shi, J.C., Dozier, J., 1995. Inferring snow wetness using C-band data from SIR-C's polarimetric synthetic aperture radar. IEEE Trans. on Geoscience and Remote Sensing 33 (4), 905–914.

Shi, J.C., Dozier, J., 1997. Mapping seasonal snow with SIR-C/X-SAR in mountainous areas. Remote Sens. Environ. 59 (2), 294–307. https://doi.org/10.1016/S0034-4257(96)00146-0.

Shi, J.C., Dozier, J., 2000a. Estimation of snow water equivalence using SIR-C/X-SAR. I. Inferring snow density and subsurface properties. IEEE Trans. on Geoscience and remote Sensing 38 (6), 2465–2474. https://doi.org/10.1109/36.885195.

Shi, J.C., Dozier, J., 2000b. Estimation of snow water equivalence using SIR-C/X-SAR. II. Inferring snow depth and particle size. IEEE Trans. on Geoscience and remote Sensing 38 (6), 2475–2488. https://doi.org/10.1109/36.885196.

Shimada, M., 2009. Advanced Land Observation Satellite (ALOS) and its follow-on satellite, ALOS-2. In: Proceedings of the 4th International PolInSAR 2009 Workshop. ESA/ESRIN, Frascati, Italy.

Shimada, M., et al., 2009. PALSAR radiometric and geometric calibration. IEEE Trans. Geosci. Remote Sens. 47 (12) (Dec 2009).

Siqueira, P., Hensley, S., Shaffer, S., Hess, L., McGarragh, G., Chapman, B., Freeman, A., 2000. A continental-scale mosaic of the Amazon Basin using JERS-1 SAR. IEEE Trans. on Geoscience and Remote Sensing 38 (6), 2638–2644.

Snoeij, P., et al., 2010. C-SAR Instrument Design for the Sentinel-1 Mission, IEEE Radar Conference 2010, Washington, DC.

Soares, J.V., Renno, C.D., Formaggio, A.R., Yanasse, C., Frery, A.C., 1997. An investigation of the selection of texture features for crop discrimination using SAR imagery. Remote Sens. Environ. 59 (2), 234–247. https://doi.org/10.1016/S0034-4257(96)00156-3.

Souyris, J.C., et al., 1995. Inversion of Landes Forest biomass using SIR-C/X-SAR data: Experiment and theory. In: Proceedings of IGARSS '95, Firenze, Italy, https://doi.org/10.1109/IGARSS.1995.521183.

Souyris, J.-C., Imbo, P., Fjørtoft, R., Mingot, S., Lee, J.-S., 2005. Compact polarimetry based on symmetry properties of geophysical media: the π/4 mode. IEEE Trans. Geosci. Remote Sens. 43 (3), 634–646.

Spencer, M., Chan, S., Veilleux, L., Wheeler, K., 2009. The Soil Moisture Active/Passive (SMAP) Mission Radar: A Novel Conically Scanning SAR, Proceedings of the 2009 IEEE Radar Conference, Pasadena, CA, USA.

Stern, R.J., Abdelsalam, M.G., 1996. The origin of the Great Bend of the Nile from SIR-C/X-SAR imagery. Science 274 (5293), 1696–1698. https://doi.org/10.1126/science.274.5293.1696.

Stofan, E.R., et al., 1995. Overview of results of spaceborne imaging radar-C, X-band synthetic aperture radar (SIR-C/X-SAR). IEEE Trans. on Geoscience and Remote Sensing 33 (4), 817–828.

Stuhr, F., Jordan, R.l., Werner, M., 1995. SIR-C/X-SAR: a multifaceted radar. In: International Proceedings International Radar Conference, Alexandria, VA, https://doi.org/10.1109/RADAR.1995.522519.

Tebaldini, S., 2010. Single and multipolarimetric SAR tomography of forested areas: a parametric approach. IEEE Trans. Geosci. Remote Sens. 48 (5), 2375–2387.

Tomiyasu, K., 1981. Conceptual performance of a satellite borne, wide swath synthetic aperture radar. IEEE Trans. Geosci. Remote Sens. (2), 108–116.

Truong-Loi, M. L., Freeman, A., Dubois-Fernandez, P., 2009. Estimation of soil moisture and Faraday rotation from bare surfaces using compact polarimetry, IEEE TGRS Vol. 47, Num. 11, pp. 3608–3615.

USGS, 2019. USGS EROS Data Center SIR-C Data Archive. https://www.usgs.gov/centers/eros/science/usgs-eros-archive-radar-spaceborne-imaging-radar-c-band-sir-c?qt-science_center_objects=0#qt-science_center_objects, Accessed date: 22 March 2019.

Villano, M., Krieger, G., Moreira, A., 2017. New insights into ambiguities in quad-Pol SAR. IEEE Trans. Geosci. Remote Sens. 55 (6), 3287–3308.

Wang, J.R., Hsu, A., Shi, J.C., O'Neill, P.E., Engman, E.T., 1997. A comparison of soil moisture retrieval models using SIR-C measurements over the little Washita River watershed. Remote Sens. Environ. 59 (2), 308–320. https://doi.org/10.1016/S0034-4257(96)00145-9.

Weeks, R., Smith, M., Pak, K., Gillespie, A., 1997. Inversions of SIR-C and AIRSAR data for the roughness of geological surfaces. Remote Sens. Environ. 59 (2), 383–396. https://doi.org/10.1016/S0034-4257(96)00161-7.

Werner, M., 2001. Shuttle Radar Topography Mission (SRTM) - mission overview. Frequenz 55 (3–4), 75–79.

Werninghaus, R., Buckreuss, S., 2009. The TerraSAR-X mission and system design. IEEE Trans. Geosci. Remote Sens. 48 (2), 606–614.

Werninghaus, R., Balzer, W., Buckreuss, S., Mittermayer, J., Mühlbauer, P., Pitz, W., 2004. The TerraSAR-X Mission, Proceedings of EUSAR 2004, Ulm, Germany.

Wright, P.A., Quegan, S., Wheadon, N.S., Hall, C.D., 2003. Faraday rotation effects on L-band spaceborne SAR data. IEEE Trans. Geosci. Remote Sens. 41 (12), 2735–2744.

Yamaguchi, Y., Moriyama, T., Ishido, M., Yamada, H., 2005. Four-component scattering model for polarimetric SAR image decomposition. IEEE Trans. Geosci. Remote Sens. 43 (8).

Yanasse, C.F., Sant'Anna, S.J.S., Frery, A.C., Renno, C., Soares, J.V., Luckman, A.J., 1997. Exploratory study of the relationship between tropical forest regeneration stages and SIR-C L and C data. Remote Sens. Environ. 59 (2), 180–190. https://doi.org/10.1016/S0034-4257(96)00149-6.

Yokota, Y. Okada, K. Iribe, M. Tsuji, A Ando, Y. Kunii, 2013. Newly developed X-band

SAR system onboard Japanese small satellite ASNARO-2, Published in: Synthetic Aperture Radar (APSAR), 2013 Asia-Pacific Conference, 23–27 Sept. 2013, Tsukuba, Japan.

de Zan, F., Monti Guarnieri, A., 2006. TOPSAR: terrain observation by progressive scans. IEEE Trans. Geosci. Remote Sens. 44 (9), 2352–2360.

Zebker, H.A., Rosen, P., Hensley, S., Mouginis-Mark, P.J., 1996. Analysis of active lava flows on Kilauea Volcano, Hawaii, using SIR-C radar correlation measurements. Geology 6, 495–498. https://doi.org/10.1130/0091-7613(1996)024<0495:AOALFO>2.3.CO;2.

Zhu, X., Bamler, R., 2010. Very high resolution spaceborne SAR tomography in urban environment. IEEE Trans. Geosci. Remote Sens. 48 (12), 4296–4308.

Zink, M., Bamler, R., 1995. X-SAR radiometric calibration and data quality. IEEE Trans. on Geoscience and Remote Sensing 33 (4), 840–847.

Zink, M., et al., 2014. TanDEM-X: the new global DEM takes shape. IEEE Geoscience & Remote Sensing Magazine 2 (2), 8–23.

Zribi, M., Taconet, O., Le Hégarat-Mascle, S., Vidal-Madjar, D., Emblanch, C., Loumagne, C., Normand, M., 1997. Backscattering behavior and simulation comparison over bare soils using SIR-C/X-SAR and ERASME 1994 data over Orgeval. Remote Sens. Environ. 59 (2), 256–266. https://doi.org/10.1016/S0034-4257(96)00158-7.

van Zyl, J.J., 1989. Unsupervised classification of scattering behavior using radar polarimetry data. IEEE Trans. on Geoscience and Remote Sensing 27 (1), 36–45.